

Supporting PtRh alloy nanoparticle catalysts by electrodeposition on carbon paper for the ethanol electrooxidation in acidic medium

Radostina V. Genova-Koleva¹, Francisco Alcaide^{1,*}, Garbiñe Álvarez¹, Pere L. Cabot²,
Hans-Jürgen Grande¹, María V. Martínez-Huerta³, Oscar Miguel¹

¹*CIDETEC, P^o Miramón, 196, 20014 Donostia-San Sebastián, Spain*

²*Laboratori d'Electroquímica de Materials i del Medi Ambient, Dept. Química Física, Universitat de Barcelona, C/ Martí i Franquès, 1-11, 08028 Barcelona, Spain*

³*Instituto de Catálisis y Petroleoquímica, CSIC, C/ Marie Curie, 2. 28049 Madrid, Spain*

*Corresponding author: Tel: +34 943 309 022, Fax: +34 943 309 136, E-mail:

falcaide@cidetec.es

Abstract

Pt₈₀Rh₂₀ and Pt₆₀Rh₄₀ alloy catalysts were electrodeposited at constant current density from different electrolytic baths on commercial carbon paper in order to be tested for the ethanol oxidation reaction (EOR) and as anodes in a direct ethanol fuel cell (DEFC). Pt and Rh anodes prepared in the same form were also examined for comparison. As measured by energy-dispersive X-ray microanalyses, the electrodeposited Pt:Rh atomic ratios were the same as those of the precursors in the bath. X-ray diffraction showed the PtRh alloy formation with mean particle sizes of 8.3 and 7.0 nm for Pt₈₀Rh₂₀ and Pt₆₀Rh₄₀, respectively, and a Pt lattice contraction caused by the Rh addition. The X-ray photoelectron spectroscopy analyses suggested a Pt lattice strain due to Rh alloying because the Pt4f binding energies were shifted to higher values with respect to that of pure Pt. The onset potentials of the alloy oxidation, CO stripping and ethanol oxidation in the cyclic and linear sweep voltammograms indicated that Pt₆₀Rh₄₀ was the most active for the CO and the ethanol electrooxidation. The apparent activation energies for the EOR on that alloy were also the lowest one, in agreement with its highest activity. These results were explained by the bifunctional mechanism, assuming that Rh contributed with hydroxylated species to favor the removal of the CO-type adsorbed species on Pt sites, and by the effect of Rh on the Pt electronic structure, the lattice strain being dominating over the charge transfer between Rh and Pt. Tests carried out in single DEFCs showed the feasibility of using the Pt₆₀Rh₄₀ electrodeposited electrodes on carbon as the anode in a real fuel cell environment.

Keywords: PtRh alloys, electrodeposition, ethanol electrooxidation, direct ethanol fuel cell, CO tolerance

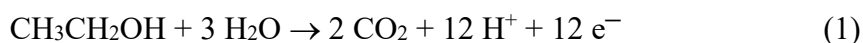
1. Introduction

The increasing industrialization using fossil fuels leads to growing environmental problems and, on the other hand, these resources are finite. Therefore, it is necessary to look for new energy sources which have to be sustainable, efficient and environmentally friendly. Fuel cells are promising candidates because of their potentially high efficiency and wide range of applications, from portable to stationary, with pollutants emission tending to zero during operation [1,2].

Direct alcohol fuel cells (DAFCs) are the most promising ones for small portable applications such as cellular phones, laptop computers, cameras and clinical devices, because of their compact and simple design, easy recharging and storage of the liquid fuel [3,4]. DAFCs are nowadays very interesting for novel microelectronic devices, which require the development and implementation of new compatible power sources able to fulfill their energy requirements [5-8].

Dealing with liquid fuels, ethanol has superior advantages due to its energy density, low toxicity and less environmental concerns in comparison to other alcohols widely studied for DAFCs, such as methanol or ethylene glycol, as it can be produced from biomass fermentation [9]. Table 1 lists the properties of some DAFCs [10,11]. However, until the date, direct ethanol fuel cells (DEFCs) have been scarcely used at micro-scale [12-14]. This can be explained by the low electrochemical activity of ethanol at the usual mild operating conditions of DEFCs, i.e. low temperature and atmospheric pressure.

The complete oxidation of ethanol to CO₂ yields 12 electrons per molecule, as follows:



Ethanol has then high energy content. However, it is a fairly complex reaction that requires the C—C bond breaking [15]. This is not easy and therefore, acetaldehyde and acetic acid are usually the dominant reaction products, which require two and four electrons, respectively, instead of twelve for reaction (1) [16-22]. Platinum, the preferred catalyst in proton exchange membrane fuel cells (PEMFCs), is not able to completely oxidize ethanol to CO₂ because its surface is easily poisoned by the intermediate reaction products [23]. In order to increase the catalytic activity and selectivity towards CO₂, different Pt-based alloys and intermetallics have been synthesized and tested [24-38]. In spite of the performance increase observed in DEFCs currently operating at temperatures between 80-120 °C, the selectivity towards CO₂ of most of these materials still remains low [39]. The most promising are the PtRh/C-based catalysts, which show an increase in the current density for the ethanol oxidation and an enhancement in the CO₂ yield under mild operating conditions ($T \leq 90$ °C) [40-47]. Thus, the CO₂ selectivity of PtRh(1:1) supported on reduced graphene oxide (RGO) was found to be more than 16 times greater than that of commercial Pt/C [22]. It was suggested that the use of PtRh with a third element could probably increase the selectivity of CO₂ [40]. However, it was only about 5 % for PtRuRh(2:1:1)/C, only something greater than that of PtRu/C (ca. 3 %), whereas that of Pt/C could reach up to about 35 % [21]. This behavior has been attributed to the role of the Rh atoms in activating the C—C bond breaking and to the modification of Pt electronic structures to lower the bonding strength with the reaction intermediates [41,47,48]. An additional bifunctional effect was ascertained with Ni addition to the Pt₇₅Rh₂₅ alloy supported on graphene nanosheets to obtain Pt₇₅Rh₁₅Ni₁₀ [47], thus improving the onset potential and current densities for ethanol oxidation.

A measurement of the activity of the different anode catalysts for ethanol oxidation may be the maximum power density provided in single DEFC together with the corresponding current density. A list of values of the literature has been collected in Table 2, classified by the catalyst, ethanol concentration, membrane and working temperature. It is shown that the cell performance increases with temperature. The highest values using Nafion membranes at 90 °C were obtained for PtSn, followed by PtRu. However, for DEFC applications not only the power density is important, but also the CO₂ selectivity in order to obtain sufficient energy density and energy conversion efficiency [21].

The results obtained with the PtRh/C catalysts make them particularly attractive for application in micro DEFCs to power small devices. On the other hand, with regards to their appropriate integration in these systems, it is necessary to consider different approaches for the miniaturization of the conventional assembly design, currently based on traditional gas diffusion electrodes [53,54]. As shown previously by the authors [55], electrodeposition offers many advantages for this purpose, leading to a good dispersion of the Pt catalyst on the membrane-electrode interface, with a precise control of the metal loading and a high catalyst utilization. In fact, electrodeposited Rh and PtRh model electrodes have been used to study different electrochemical reactions such as nitrate reduction in neutral medium [56] and oxidation of small organic molecules [57-59]. However, in the best of authors' knowledge, no attempts have been made to prepare DEFC anodes by means of PtRh electrodeposition using impressed current. This procedure could simplify the fabrication process of microdevices.

In this work carbon-supported PtRh electrodes have been prepared by a simple and readily scalable electrodeposition technique using industrial electrolytic baths. Several PtRh electrodes having different Pt:Rh atomic ratios have been obtained by

electrodeposition from electrolytic baths with different formulations in order to study the effect of the Pt:Rh atomic ratio. The physical and electrochemical characterization towards ethanol oxidation in acidic media was carried out using cyclic voltammetry (CV), linear sweep voltammetry (LSV), and chronoamperometry (CA). Finally, the performance of the prepared PtRh anodes was assessed in single DEFCs.

2. Materials and methods

2.1. Reactants

All chemicals used in this work were of RG quality and the aqueous solutions were prepared using ultrapure water ($\kappa \leq 0.54 \mu\text{S cm}^{-1}$) obtained from a Millipore Milli-Q system. The reactants were $\text{H}_2\text{PtCl}_6 \cdot 6\text{H}_2\text{O}$ (Alfa Aesar), $\text{RhCl}_3 \cdot 3\text{H}_2\text{O}$ (Sigma-Aldrich), and ethanol and H_2SO_4 (Merck).

2.2. Preparation of the catalyzed electrodes

The electrodeposition was performed in a thermostatically controlled two-compartment glass cell at $25 \pm 1 \text{ }^\circ\text{C}$. A platinized titanium mesh was used as a counter electrode (CE). The different working electrodes (WEs) were prepared by galvanostatic deposition of Pt, Rh and co-deposition of Pt and Rh onto a microporous carbon layer that covered a porous carbon paper (H2315 I2 C6, thickness $255 \mu\text{m}$ from Freudenberg Inc.). These WEs were placed in a home-made sealed frame with the carbon paper side being connected to a Pt-coated current collector, whereas the catalyzed side, 5 cm^2 in section, was in contact with the electroplating bath, which contained the appropriate (stoichiometric) amounts of $\text{H}_2\text{PtCl}_6 \cdot 6\text{H}_2\text{O}$ (10 mM) and $\text{RhCl}_3 \cdot 3\text{H}_2\text{O}$ in N_2 -purged 1.0 mol dm^{-3} H_2SO_4 solution [60]. The Rh^{3+} ion concentrations used here were relatively low to avoid the metal deposition limitations due to the formation of rhodium complexes at high concentrations previously described in the literature [59]. In addition, the microporous carbon layer used should be in principle sufficiently conductive to

facilitate Rh deposition, thus avoiding possible problems for Rh deposition on little conductive supports [61]. All electrodepositions were performed at a current density of 0.020 A cm^{-2} for 300 s, using a PGSTAT 30 potentiostat/galvanostat (Eco Chemie). Once prepared, the catalyzed electrodes were gently rinsed with abundant ultrapure water to remove possible ionic species coming from the electrolytic bath.

2.3. Physico-chemical and electrochemical characterization

The electrodeposited catalytic layers were characterized by field emission scanning electron microscopy (FE-SEM) using a Zeiss Ultra Plus microscope, and X-ray diffraction (XRD) by means of a Bruker D8 Advance diffractometer equipped with a Cu K_α source ($\lambda = 1.5406 \text{ \AA}$). The elemental composition of these catalytic layers was determined by energy dispersive X-ray (EDX) microanalysis, using an INCA-300 energy analyzer coupled to a scanning electron JSM5910-LV JEOL microscope. The reported microanalyses data correspond to the mean values obtained from measurements at 10 different points in each sample. X-ray photoelectron spectroscopy (XPS) analyses were performed in order to get information on the chemical state and relative concentration of surface species. The XPS spectra were obtained with a VG Escalab 200R spectrometer equipped with a hemispherical electron analyzer (constant pass energy of 50 eV) and a Mg K_α ($h\nu = 1254.6 \text{ eV}$) X-ray source, powered at 120 W. The XPS data signals were taken in increments of 0.1 eV with dwell times of 50 ms. Binding energies were calibrated relative to the C 1s peak at 284.6 eV. The high resolution spectra envelopes were obtained by fitting of the peak components using the *XPS peak* software. Symmetric Gaussian-Lorentzian product functions were used to approximate the line shapes of the fitting components.

The electrochemical characterization of the catalyzed electrodes (0.79 cm^2 in section) was carried out in a thermostated three-electrode glass cell with two compartments. The

WE was located inside a cylindrical holder, whose rear side had an inlet and an outlet allowing the circulation of liquid and gases, to mimic the anode setup in the fuel cell. A Pt wire separated from the main electrolyte by a glass frit served as the CE, whereas the reference electrode (RE) was the Hg|Hg₂SO₄|K₂SO₄(sat) (MSE) electrode immersed in glass tube ended with a Luggin capillary. However, all the electrode potentials given in this paper are referred to the reversible hydrogen electrode (RHE). Deoxygenated aqueous 0.50 mol dm⁻³ H₂SO₄ solution was used in all cases as electrolyte. The oxidation activity of the electrodeposited catalysts was studied in 2.0 mol dm⁻³ ethanol + 0.50 mol dm⁻³ H₂SO₄.

The electrochemical tests were performed at 25 °C using a potentiostat/galvanostat PGSTAT 30 (Eco Chemie) controlled by the GPES software. Cyclic voltammograms were recorded in a potential range between 0.05-1.0 V vs. RHE at a sweep rate of 20 mV s⁻¹ until they were reproducible. The linear sweep voltammograms were obtained at 1 mV s⁻¹. Steady-state potentiostatic data were recorded at 0.500 V vs. RHE for 30 min in the acidic 2.0 mol dm⁻³ ethanol solution. CO stripping voltammetry was performed feeding the working electrode with a mixture of 0.1 % CO in N₂ (99.999 %, Praxair) at 0.250 cm³ min⁻¹ and atmospheric pressure for 50 min, while holding the electrode potential at 0.100 V vs. RHE. After the adsorption, the non-adsorbed CO was removed from the solution by N₂ bubbling for 30 min, still holding the admission potential. Then, two CO stripping voltammograms were recorded in the positive direction from 0.050 to 1.20 V vs. RHE at 20 mV s⁻¹. To compare the intrinsic activities of the catalysts, the currents measured for a given catalysts were normalized to the charges needed for the corresponding CO stripping, which is proportional to the respective number of active sites [62].

2.4. Fuel cell tests

The fuel cell testing was carried out in a 5 cm² DEFC single cell hardware (Fuel Cell Technologies) connected to a potentiostat 1287A (Solartron Analytical, Inc.). Membrane electrode assemblies (MEAs) were prepared by the hot-pressing method [63]. Electrodes made of the commercial carbon paper mentioned before with an electrodeposited metal loading of 1.0 mg cm⁻² were used as the anodes, while the cathodes were made from commercial Pt black (E-Tek, Inc.), sprayed to a loading of 4.0 mg_{Pt} cm⁻² onto a commercial gas diffusion layer ELAT 1400 LT (NuVant Systems Inc.). Each MEA was assembled sandwiching the anode and the cathode on either side of the Nafion[®] 115 membrane at 50 bar and 130 °C for 180 s. The cell performance was evaluated recording steady-state potentiodynamic *V-j* curves at a scan rate of 5 mV s⁻¹ at constant flow-rate mode. The cell temperature (*T*_{cell}) was between 40 and 90 °C. The anode was fed with an acidic 2.0 mol dm⁻³ ethanol aqueous solution at 1.5 mL min⁻¹ and atmospheric pressure, preheated up to *T*_{cell}. The cathode was fed with pure O₂ (99.999 %, Praxair) from cylinders at 50 standard cubic centimeters per minute (sccm), humidified at 70 °C and atmospheric pressure.

3. Results and Discussion

3.1. Physico-chemical characterization

The FE-SEM images and EDX microanalyses of the microporous carbon layers, after the electrodeposition of the different catalysts, showed the porosity of the surface and the homogeneous dispersion of the corresponding metals. Selected FE-SEM images of the carbon paper catalyzed by Pt, Pt₈₀Rh₂₀, Pt₆₀Rh₄₀ and Rh are shown in Fig. 1a-d, respectively. It can be observed many small hemispherical clusters, and there is some secondary growth in form of elongated leaf-like flake aggregations. The relative Pt:Rh atomic ratios on the electrodeposited electrodes were determined from EDX and listed in Table 3. The real bulk compositions obtained by this technique were Pt_{80.4}Rh_{19.6} and

Pt_{62.4}Rh_{37.6} for the nominal Pt:Rh atomic ratios of 80:20 and 60:40, respectively. The experimentally measured values were then very close to the nominal (stoichiometric) ones, thus meaning that the conductivity of the support and the concentrations used of the rhodium precursor were suitable to avoid the Rh electrodeposition limitations previously described [59,61].

The electrodeposited catalysts containing different atomic percentages of Rh were also characterized by XRD. The respective diffractograms have been depicted in Fig. 2. Typical diffraction peaks of face-centered cubic (*fcc*) crystalline structure of Pt were found for all the catalysts, which correspond to (111), (200), (220) and (311) planes [59,61]. The characteristic peaks corresponding to pure Pt can be seen at $2\theta = 39.9^\circ$, 46.4° , 67.7° and 81.6° , respectively. A close inspection of the peaks reveals that reflections for PtRh alloy surfaces are shifted to higher angles with increasing the Rh content. For example, in the case of (111) peaks at $2\theta = 39.90^\circ$, 40.09° , 40.29° and 41.20° for Pt, Pt₈₀Rh₂₀, Pt₆₀Rh₄₀ and Rh, respectively, were found. This angle increase in the peak position can be explained by a lattice contraction with an increasing amount of Rh, because the latter has an atomic radius of 1.73 Å, smaller than that of Pt, which is of 1.77 Å [41]. In order to test whether PtRh alloy was completely formed or there was a segregation of the constituent elements, Vegard's law was applied [42]:

$$a_{\text{PtRh}} = (1-x_{\text{Rh}}) a_{\text{Pt}} + x_{\text{Rh}} a_{\text{Rh}} \quad (2)$$

where a_{PtRh} , a_{Pt} and a_{Rh} are the lattice parameters of the PtRh alloy, assumed as a solid solution, and those of pure Pt and Rh metals, respectively, whereas x_{Rh} is the molar fraction of Rh in such a solid solution. Table 3 lists the experimental lattice parameters together with those calculated from Vegard's law (theoretical values), taking into account the indicated experimental lattice parameters for pure Pt and Rh together with the bulk composition values obtained from EDX analyses. The experimental and

theoretical data thus obtained are in a good agreement within the experimental error, thus suggesting the complete PtRh alloy formation as a solid solution in the present electrodeposition conditions. The formation of PtRh solid solutions using different procedures has also been suggested by other authors [59,61].

The mean crystallite sizes were estimated from the Scherrer equation:

$$\tau = K \lambda / \beta \cos \theta \quad (3)$$

where K is a dimensionless shape factor with a value close to unity (typical value of about 0.9), λ is the X-ray wavelength, β (in radians) is the line broadening at full width at half maximum (FWHM) after subtracting the instrumental line broadening and θ is the Bragg angle. The corresponding values are also listed in Table 3.

The general survey of the XPS analyses allowed obtaining the relative composition in Pt and Rh of the electrodeposited catalysts. The compositional results thus obtained are compared to the nominal ones in Table 4. They are referred to be the surface results because the depth analyzed by this technique is smaller than that analyzed by EDX. These values are not far from the nominal ones, suggesting a slight surface Pt enrichment. However, they are comparable to those obtained by EDX (see Table 3) and therefore, in agreement with the formation of a PtRh solid solution during the electrodeposition. On the other hand, the high resolution spectra of the Pt 4f and Rh 3d regions are depicted in Fig. 3. Figs. 3a and b correspond to the pure metals, Pt and Rh, respectively, whereas Figs. 3c and d, to Pt₈₀Rh₂₀, and Figs. 3e and f, to Pt₆₀Rh₄₀. In all cases, the oxidation states of Pt, as Pt(II), and of Rh, as Rh(III), had to be considered for a suitable peak deconvolution.

The Pt⁰ 4f spectra of Pt showed a higher binding energy (BE) of Pt 4f_{5/2} at 74.8 eV and a lower BE energy of Pt 4f_{7/2} at 71.5 eV (Fig. 3a). The Pt⁰ 4f_{7/2} BEs for both, Pt₈₀Rh₂₀ and Pt₆₀Rh₄₀, were located at 71.7 eV (Figs 3c and e). The BEs of Rh⁰ 3d_{5/2} and

$3d_{3/2}$ for pure Rh were located at 307.6 eV and 312.4 eV, respectively (Fig. 3b). The BEs of $Rh^0 3d_{5/2}$ for both, $Pt_{80}Rh_{20}$ and $Pt_{60}Rh_{40}$, were found at 307.4 eV (Figs. 3d and f). There was only a small shift of about 0.2 eV in the Pt and Rh BEs when alloying both metals. Note, however, that these shifts for Pt and Rh were opposite. Small shifts were also found for the Pt(II) $4f_{5/2}$, from 73.5 eV for Pt to 73.7-74.0 eV for $Pt_{80}Rh_{20}$ and $Pt_{60}Rh_{40}$ (Figs. 3a, c and e). On the other hand, those corresponding to the Rh(III) $3d_{5/2}$ peaks for $Pt_{80}Rh_{20}$ and $Pt_{60}Rh_{40}$ were more difficult to precisely determine because of the dominant Pt $4d_{5/2}$ peak (see Figs. 3b, d and f). These results, in agreement with those reported previously for PtRh alloys supported on graphene nanosheets [47] and for mixed metals and alloyed surfaces on graphite [64] for ethanol and CO electrooxidation, can be interpreted by changes in the electronic properties of the atoms involved such as those produced by charge transfer between elements and lattice strain [47,65]. In the case of charge transfer from Rh to Pt, as previously suggested for PtRh alloys [47] (although they have the same electronegativity of 2.28), a decrease in the Pt BEs would be expected, what it is not seen in the XPS spectra. However, the incorporation of alloying atoms such as Rh, Ni and Ru ones can produce compressive strains in the Pt lattice due to the lattice contraction, thus leading to an increase in the binding energies of Pt [47,66]. In our case there is evidence of such a lattice strain because of the lattice parameter decrease for the PtRh alloys (Table 3), thus explaining the net shift of the Pt BEs to higher values when it is alloyed with Rh. This means that lattice strain dominates over charge transfer to produce a net shift of the Pt BEs towards higher values when alloying with Rh.

Measuring the areas of the peaks corresponding to the metallic and oxidized states of Pt and Rh species, the relative atomic percentages of the metallic and the oxidized state of each element was determined and the respective results are also listed in Table 4. The

presence of metallic Pt⁰ is essential for providing sites for alcohol adsorption and electrooxidation, whereas Rh oxides would facilitate the CO oxidation [64].

3.2. CO electrooxidation

Fig. 4 presents the stabilized cyclic voltammograms corresponding to the PtRh catalysts in deaerated 0.50 mol dm⁻³ H₂SO₄. The cyclic voltammogram corresponding to Pt (curve *a*) shows the typical features observed in polycrystalline Pt in acidic electrolyte [67]. In the anodic scan, the atomic hydrogen desorption peaks appear at potentials in the range 0.050–0.40 V, the double layer region between 0.40 and 0.60 V, and the Pt oxide formation starts at about 0.60 V. In the reverse scan, the Pt oxide reduction peak is located at about 0.8 V and the atomic adsorption peaks appear also in the range 0.050–0.40 V. The voltammetric profile of Rh (curve *d*) is like that of Pt although with some changes in the potential range values where the processes take place. In the anodic scan the hydrogen desorption peak appears at potentials between 0.050 and 0.30 V and then, Rh oxidation takes place. In the reverse scan the Rh oxide reduction peak is centered at about 0.45 V and the atomic H adsorption takes place in the same potential region as H desorption. Note that both, Rh oxide formation and reduction, occur at potentials lower than those corresponding to Pt oxide formation and reduction, respectively. The voltammetric response of Pt₈₀Rh₂₀ and Pt₆₀Rh₄₀, curves *b* and *c* in Fig. 4, respectively, show a mixed profile, which involves platinum and rhodium as expected for PtRh alloys [58]. The oxidation of Pt₈₀Rh₂₀ and Pt₆₀Rh₄₀ begins at much less positive potentials than that observed for pure Pt, *ca.* 0.38 and 0.36 V, respectively. On the other hand, they were greater than that *ca.* 0.30 V for the Rh oxidation (Table 5), which suggests a charge transfer from Rh to Pt. In addition, the peaks corresponding to the reduction of oxides shift towards more negative potentials

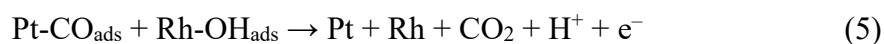
when the Rh content in the alloy increases. The onset potentials for the oxidation of these catalysts have been listed in Table 5.

Fig. 5 depicts the CO stripping experiments and illustrates the performance of the catalysts for the CO electrooxidation. It is clearly shown that there is a significant shift of the onset potentials for CO oxidation on Rh and PtRh electrodes to less positive values when compared to the onset potential for CO oxidation on Pt, which is about 0.69 V (see Table 5). The onset potential for CO oxidation on Rh is about 0.59 V (curve *d* in Fig. 5). This can be explained by the formation of oxidized Rh species at potentials lower than that of Pt, as can be seen in Fig. 4 (curves *a* and *d*). It has been pointed out that the Rh-O bonding is stronger than that of Pt-O [40]. For this reason it is probably the surface hydroxide formation on Rh the way in which adsorbed CO on this metal is easier oxidized than on Pt. Considering two neighboring Rh atoms, the CO₂ formation may be represented as follows:



where Rh-OH_{ads} means OH adsorbed on Rh metal or on oxidized Rh. When alloying Pt with Rh to form the Pt₈₀Rh₂₀ catalyst, the onset potential for CO oxidation, curve *b* in Fig. 5, is also more negative than those of pure Pt and Rh, with values of 0.50 and 0.45 V for Pt₈₀Rh₂₀ and Pt₆₀Rh₄₀, respectively (Table 5), i.e. in the potential region corresponding to Rh oxidation (Fig. 4). To explain this, a new feature in addition to the hydroxide adsorption on the Rh species must be considered. The effect of the electronic structure of Pt on its catalytic activity has been generally interpreted with the help of the d-band theory [47,68,69]. According to this theory, the downshift of the d-band center of Pt with respect to the Fermi level would lead to a reduction of the bonding strength with the adsorbates. This electronic effect can be due to a lattice strain (geometric effect) and to charge transfer between atoms (ligand effect). As discussed before in this

paper (see Fig. 3), the slight opposite shifts of the Pt 4f and Rh 3d bands in the PtRh alloys can be assigned to the electronic effect of Rh on Pt (geometric, not ligand one) and therefore, a decrease in the Pt-CO bond strength is predicted, in agreement with previous results in the literature [40,41,47]. For this reason, the Pt-CO bond strength in the PtRh alloy appears to be weaker than that corresponding to pure Pt and Rh and therefore, CO should be easier oxidized on Pt according to the bifunctional mechanism:



thus explaining that the anodic currents on Pt₈₀Rh₂₀ are greater than those on pure Rh for potentials before the onset potential for CO oxidation on the latter. On the other hand, the greatest anodic currents were found for Pt₆₀Rh₄₀, also for potentials well before the onset potential of CO stripping on pure Rh. In this case, the Rh at.% of the alloy is greater than in Pt₈₀Rh₂₀ and then, the greater amount of Rh-OH_{ads} species, together with the electronic effect mentioned before, can explain the greatest CO stripping currents achieved.

3.3. Ethanol electrooxidation

Fig. 6 depicts the cyclic voltammograms corresponding to the ethanol oxidation reaction (EOR) on the PtRh alloys studied at 20 mV s⁻¹ and 25 °C. As shown in this figure, there are big differences in the anodic currents on the different electrodeposited electrodes. The Pt-based catalysts produce a significant ethanol oxidation, whereas Rh is scarcely active. Another significant point is that the anodic currents on the Pt-based catalysts during the cathodic sweep cross over those obtained during the anodic scan. This is related to the limited oxidation of ethanol and the reaction intermediates in the direct sweep, which continue to be oxidized in the reverse scan. In addition the height of the anodic peak in the reverse scan in Pt₈₀Rh₂₀ is greater than that in the direct one.

Conversely, it is smaller for Pt₆₀Rh₄₀, thus meaning that the intermediates are easier removed in the latter than in the case of Pt₈₀Rh₂₀.

Fig. 7 shows the electrocatalytic activities of Pt, Pt₈₀Rh₂₀, Pt₆₀Rh₄₀ and Rh electrodes for the EOR by linear sweep voltammetry at 1.0 mV s⁻¹ and 60 °C. Note that they are referred to the overall CO stripping charge to normalize with respect to the amount of electroactive sites, as indicated in the experimental part. The onset potentials for the ethanol oxidation on the different catalysts have also been listed in Table 5. It is shown that ethanol starts being oxidized at about 0.60 and 0.57 V on Pt and Rh, respectively, but for Pt₈₀Rh₂₀ and Pt₆₀Rh₄₀, the corresponding onset potentials are less positive, 0.46 and 0.44 V. This leads to higher specific current densities at lower overpotentials for the PtRh alloys, curves *b* and *c*, compared to pure Pt and Rh electrodes, curves *a* and *d*, respectively. It is clearly shown that the best activity for the ethanol oxidation corresponds to Pt₆₀Rh₄₀, as in the case of the CO oxidation (Fig. 5).

The different activities for the ethanol electrooxidation can also be evidenced by determining the corresponding activation energies. The effect of the temperature on the EOR kinetics on the Pt, Pt₈₀Rh₂₀, Pt₆₀Rh₄₀ and Rh catalyzed electrodes was studied in the temperature range from 20 to 70 °C also in 2.0 mol dm⁻³ ethanol + 0.50 mol dm⁻³ H₂SO₄. The form of the linear sweep voltammograms at different temperatures was essentially the same as that shown in Fig. 7. However, the current density increased with temperature in all the potential range, as can be seen in the example depicted in Fig. 8a for Pt₆₀Rh₄₀.

From these *E-I* curves, the corresponding ln (*I*) vs. *T*⁻¹ (Arrhenius-type) plots at constant potential *E* = 0.600 V vs. RHE (at 25.0°C), were obtained (see Fig. 8b). Good straight lines with linear regression coefficient *r* ≥ 0.999 were always found, thus indicating that the thermojunction potential between the solutions of working and

reference compartments was negligible. The plots of Fig. 8b allow determining the apparent activation energy at $E = 0.600$ V, $U_{\text{app}}^{\#}(E)$, since the slope of Arrhenius-type plots can be taken as $-U_{\text{app}}^{\#}(E) / R$ [70], where R is the gas constant ($8.314 \text{ J K}^{-1} \text{ mol}^{-1}$). The apparent activation energies for the ethanol electrooxidation are listed in Table 5 and are in decreasing order: $\text{Rh} > \text{Pt} > \text{Pt}_{80}\text{Rh}_{20} > \text{Pt}_{60}\text{Rh}_{40}$. The highest apparent activation energy for Rh is in agreement with its scarce ethanol oxidation shown in Figs. 6 and 7. The addition of Rh to Pt lowers the apparent activation energy, showing again that $\text{Pt}_{60}\text{Rh}_{40}$ is the most active.

Several values of the apparent activation energies for the EOR on different Pt and PtRh-catalyzed supports have been previously reported in the literature [22,71,72]. From these papers, apparent activation energies at 0.600 V vs. RHE have been collected. Thus, Delpeuch *et al.* [71] obtained $U_{\text{app}}^{\#}$ values of 25 ± 2 and $13 \pm 2 \text{ kJ mol}^{-1}$ for Pt/C and $\text{Pt}_1\text{Rh}_{1.6}/\text{C}$ catalysts, respectively, from steady-state current measurements in $0.10 \text{ M ethanol} + 0.50 \text{ M H}_2\text{SO}_4$. Zhu *et al.* [22], from cyclic voltammograms recorded between 25 and $65 \text{ }^\circ\text{C}$ for commercial Pt/C ($20 \text{ wt.}\%$) and $\text{Pt}_1\text{Rh}_1/\text{RGO}$ in $0.1 \text{ M ethanol} + 0.1 \text{ M HClO}_4$, estimated $U_{\text{app}}^{\#}$ values of 54 and 29 kJ mol^{-1} , respectively. From potentiodynamic measurements at temperatures in the range 10 - $70 \text{ }^\circ\text{C}$ using $1.0 \text{ M ethanol} + 0.50 \text{ M H}_2\text{SO}_4$ and carbon-supported Pt and $\text{Pt}_{74}\text{Rh}_{26}$, Sen Gupta and Datta [59] obtained $U_{\text{app}}^{\#}$ values of 42 and 28 kJ mol^{-1} , also respectively. On the other hand, Rao *et al.* [72] reported a value of 31 kJ mol^{-1} , estimated from the faradaic currents for ethanol electrooxidation in the temperature range from 30 to $90 \text{ }^\circ\text{C}$ on Pt/C ($40 \text{ wt.}\%$), in membrane electrode assembly configuration with 0.1 M ethanol . The values of the apparent activation energies obtained in this work are then comparable to those previously reported in the literature for similar systems.

As depicted in Fig. 9, the same trend as in the linear sweep voltammograms was observed for the chronoamperograms obtained at 0.500 V in 2.0 mol dm⁻³ ethanol + 0.5 mol dm⁻³ H₂SO₄ at the same temperature of 60 °C, also normalized to the overall CO stripping charge. These longer term experiments allow studying the ethanol self-poisoning oxidation reaction. It is shown that the current completely decays after the first 100-200 seconds on pure Pt and Rh. This phenomenon appears to be related to the decrease in the EOR rate due to the adsorption of stable intermediate species, which block the active sites and avoids further ethanol oxidation on them. However, when alloying Rh with Pt both, the catalytic activity and the stability of the electrode is very much improved, the best results being for Pt₆₀Rh₄₀.

According to these results, there is a significant effect of the Rh content in the alloy. The performance for the EOR increases from Pt < Pt₈₀Rh₂₀ < Pt₆₀Rh₄₀. It passes through a maximum because performance decreases to pure Rh. This indicates that there is an optimal relation between Pt and Rh and that comparable amounts of Pt and Rh atoms are needed in the alloy for an efficient ethanol electrooxidation. This suggests that neighboring Pt and Rh atoms play a key role in the activation and cleavage of the C-C bond to lead to an increased CO₂ production [40-42,61].

The EOR kinetics on the different catalysts follow the same trend as in the case of the CO oxidation and therefore, their different catalytic activity can be interpreted in the same form, considering the bifunctional and electronic effects [40,41,47,66,68]. On one hand, the lattice contraction of Pt due to alloying with Rh together with the possible charge transfer from Rh to Pt can lower the bonding strength of Pt with the reactants and the reaction intermediates; on the other, Rh is oxidized at potentials more negative than Pt and therefore, it can contribute to the easier oxidation of ethanol and of the CO-

type intermediates adsorbed on Pt by the bifunctional mechanism represented by reaction (5).

3.4. Fuel cell testing

Fig. 10 depicts the stationary voltage and specific power density vs. the specific current density curves showing the performance of the MEAs prepared with Pt black cathodes and the electrodeposited Pt₈₀Rh₂₀ (curve *a*) and Pt₆₀Rh₄₀ (*b*) catalysts on the carbon paper to a loading of 1 mg_{PtRh} cm⁻² as the anodes at 90 °C. The anode was fed with aqueous 2.0 M ethanol, while the cathode was fed with pure O₂ to maximize its activity and to reduce possible cathode effects on the relative activities of the MEAs. The different performance achieved by both MEAs is apparent. An increase in the open circuit voltage (OCV) as well as in the performance when Pt₆₀Rh₄₀ instead of Pt₈₀Rh₂₀ was used as the anode can be clearly observed. Thus, the maximum power given by the MEA with the Pt₆₀Rh₄₀ anode is 6.0 mW mg_{PtRh}⁻¹ (at 47 mA mg_{PtRh}⁻¹), which is much higher than that of 0.27 mW mg_{PtRh}⁻¹ (at 2.6 mA mg_{PtRh}⁻¹) obtained for Pt₈₀Rh₂₀. This difference has to be assigned to the catalyst composition of the anode because all the variables as well as the manufacturing method were the same for both types of MEAs. The performance of the alloy catalysts in single DEFC followed the same order of activity as that found for ethanol oxidation in the three-electrode cell experiments.

The effect of the temperature on the DEFC performance was also studied in single cell, using the MEA with Pt₆₀Rh₄₀, which yielded the best performance at 90 °C. As shown in Fig. 11, the fuel cell performance increased significantly with temperature, from a maximum specific power density of 0.34 mW mg_{PtRh}⁻¹ at 40 °C to 6.0 mW mg_{PtRh}⁻¹ at 90 °C. Taking into account that the metal loading is 1 mg_{PtRh} cm⁻², the maximum power density at 90°C is about 6 mW cm⁻², with a corresponding current density of 50 mA cm⁻². These values are relatively low, but they are in the same order of

magnitude than those obtained for Pt and PtRh (see Table 2) and they could be tuned to increase the performance parameters. The work performed in this paper shows the feasibility of electrodeposition as a suitable technique to produce micro DEFCs that could power microdevices with a facilitated fabrication process. We feel that these results are promising and encouraging for a following step in which the catalyst composition, even with third elements, the nanoparticle size and the metal loading on the anode would be optimized.

4. Conclusions

Electrodeposited PtRh catalysts containing different at. % Rh from 0 to 100, namely Pt, Pt₈₀Rh₂₀, Pt₆₀Rh₄₀ and Rh, were manufactured by galvanostatic deposition on commercial carbon paper. The SEM and EDX microanalyses showed homogenous dispersion of the catalysts on the carbon paper and that the composition of electrodeposited PtRh coincided with that of the electrodeposition bath. The crystallite size of the nanoparticles varied from 10.5 to 6.1 nm, values corresponding to pure Pt and Rh, respectively, the crystallite size decreasing when increasing the Rh content. The XRD diffractograms allowed confirming that the PtRh catalysts were electrodeposited as alloys. The XPS analyses showed a slight increase in the binding energy of Pt together with the equivalent slight decrease of the BE of Rh in the PtRh alloy. This was assigned to a Pt lattice strain produced by the Rh incorporation, because the lattice parameter decreased when increasing the Rh content, the lattice strain dominating over charge transfer.

The onset potentials for the oxide formation in the CV experiments depended on the alloy, in the order: Pt > Pt₈₀Rh₂₀ > Pt₆₀Rh₄₀ > Rh, which was assigned to the electronic effect of Rh on Pt. The onset potentials for CO oxidation were slightly different: Pt > Rh > Pt₈₀Rh₂₀ > Pt₆₀Rh₄₀, the latter being then the most active. As the onset potentials

for CO oxidation were slightly higher than those of the alloy oxidation, it was interpreted that CO removal was facilitated by the bifunctional mechanism. In addition, the decrease of the onset potential for the CO oxidation on Pd₈₀Rh₂₀ and Pd₆₀Rh₄₀ with respect to Rh was also interpreted by the electronic effect of Rh on Pt.

In the case of the EOR, the onset potential for the ethanol oxidation followed the same order as in the case of CO. The Pt₆₀Rh₄₀ alloy was again the most active, giving the highest specific current densities in the linear sweep voltammograms with the lowest apparent activation energy, which decreased in the order: Rh > Pt > Pt₈₀Rh₂₀ > Pt₆₀Rh₄₀. As in the case of CO, this was also explained by the bifunctional mechanism and the effect of Rh on the Pt electronic structure. In both cases, CO and ethanol, the highest activity appeared for comparable amounts of Pt and Rh in the nanoparticles, which could favor the bifunctional mechanism and the electronic effect of Rh on Pt.

The feasibility of the use of electrodeposited PtRh alloys supported on carbon electrodes as anodes in DEFC was demonstrated with the use of the Pt₆₀Rh₄₀ alloy in real fuel cells at temperatures from 40 to 90 °C. The maximum power densities and the corresponding current densities were of the same order of magnitude as those for Pt and PtRh alloys reported in the literature, thus encouraging further work to optimize the nanoparticle size, the anode metal loading and the catalyst composition, even with third elements, to increase the DEFC performance.

Acknowledgments

The authors gratefully acknowledge financial support given by the Spanish MINECO under project MAT2008-06631-C03-03.

5. References

- [1] D. Stolten, R.C. Samsun, N. Garland (Eds.), Fuel cells: Data, Facts and Figures, Wiley-VCH, Weinheim, 2016.
- [2] The Fuel Cell Industry Review 2018. <http://www.fuelcellindustryreview.com/> (accessed 09 May 2019)
- [3] M.Z.F. Kamarudin, S.K. Kamarudin, M.S. Masdar, W.R.W. Daud, Review: Direct Ethanol Fuel Cells, *Int. J. Hydrogen Energy* 38 (2013) 9438–9453. <https://doi.org/10.1016/j.ijhydene.2012.07.059>
- [4] C. Lamy, C. Coutanceau, J.-M. Léger, The Direct Ethanol Fuel Cell: a Challenge to Convert Bioethanol Cleanly into Electric Energy, in: P. Barbaro, C. Bianchini (Eds.), *Catalysis for sustainable energy production*, Wiley-VCH Verlag GmbH & Co. KGaA, Weinheim, 2009, pp. 3–46.
- [5] S. Tanaka, Fuel cells and their components based on microsystem technology, *WENE* 2 (2013) 350–362. <https://doi.org/10.1002/wene.68>
- [6] G. Scotti, P. Kanninen, V.-P. Matilainen, A. Salminen, T. Kallio, Stainless steel micro fuel cells with enclosed channels by layer additive manufacturing, *Energy* 106 (2016) 475–481. <https://doi.org/10.1016/j.energy.2016.03.086>
- [7] S.-S. Hsieh, H.-C. Wu, B.-S. Her, Design, fabrication and characterization of micro-electro mechanical system based micro direct methanol fuel cell stacks, *Sensors and Actuators A: Phys.* 187 (2012) 57–66. <https://doi.org/10.1016/j.sna.2012.08.026>
- [8] C. Yunphuttha, W. Bunjongpru, S. Porntheeraphat, A. Wongchaisuwat C. Hruanun, A. Poyai, P. Viravathana, Fabrication of a micro-direct methanol fuel cell using microfluidics, *Chem. Pap.* 66 (2012) 1137–1145. <https://doi.org/10.2478/s11696-012-0230-7>

- [9] C. Lamy, E.M. Belgsir, J.-M. Léger, Electrocatalytic oxidation of aliphatic alcohols: application to the direct alcohol fuel cell (DAFC), *J. Appl. Electrochem.* 31 (2001) 799–809. <https://doi.org/10.1023/A:1017587310150>
- [10] U.B. Demirci, Direct liquid-feed fuel cells: Thermodynamic and environmental concerns, *J. Power Sources* 169 (2007) 239–246. <https://doi.org/10.1016/j.jpowsour.2007.03.050>
- [11] B.C. Ong, S.K. Kamarudin, S. Basri, S. Direct liquid fuel cells: A review, *Int. J. Hydrogen Energy* 42 (2017) 10142–10157. <https://doi.org/10.1016/j.ijhydene.2017.01.117>
- [12] R.W. Verjullo, F. Alcaide, G. Álvarez, N. Sabaté, N. Torres-Herrero, J.P. Esquivel, J. Santander, A micro alkaline direct ethanol fuel cell with platinum-free catalysts, *J. Micromech. Microeng.* 23 (2013) 115006. <https://doi.org/10.1088/0960-1317/23/11/115006>
- [13] R.I. Jafri, S. Ramaprabhu, Multi walled carbon nanotubes based micro direct ethanol fuel cell using printed circuit board technology, *Int. J. Hydrogen Energy* 35 (2010) 1339–1346. <https://doi.org/10.1016/j.ijhydene.2009.11.067>
- [14] S. Aravamudhan, A.R.A. Rahman, S. Bhansali, Porous silicon based, orientation independent, self-priming micro direct ethanol fuel cell, *Sensors and Actuators A: Phys.* 123–124 (2005) 497–504. <https://doi.org/10.1016/j.sna.2005.03.069>
- [15] T. Iwasita, E. Pastor, A DEMS and FTIR spectroscopic investigation of adsorbed ethanol on polycrystalline platinum, *Electrochim. Acta* 39 (1994) 531–537. [https://doi.org/10.1016/0013-4686\(94\)80097-9](https://doi.org/10.1016/0013-4686(94)80097-9)
- [16] G.A. Cámara, T. Iwasita, Parallel pathways of ethanol oxidation: the effect of ethanol concentration, *J. Electroanal. Chem.* 578 (2005) 315–321. <https://doi.org/10.1016/j.jelechem.2005.01.013>

- [17] S. Rousseau, C. Coutanceau, C. Lamy, J.-M. Léger, Direct ethanol fuel cell (DEFC): electrical performances and reaction products distribution under operating conditions with different platinum-based anodes, *J. Power Sources* 158 (2006) 18–24. <https://doi.org/10.1016/j.jpowsour.2005.08.027>
- [18] S.C. Zignani, V. Baglio, J.J. Linares, G. Monforte, E.R. Gonzalez, A.S. Aricò, Performance and selectivity of Pt_xSn/C electro-catalysts for ethanol oxidation prepared by reduction with different formic acid concentrations, *Electrochim. Acta* 70 (2012) 255-265. <https://doi.org/10.1016/j.electacta.2012.03.055>
- [19] S.C. Zignani, V. Baglio, D. Sebastián, S. Siracusano, A.S. Aricò, Enhancing ethanol oxidation rate at PtRu electro-catalysts using metal-oxide additives, *Electrochim. Acta* 191 (2016) 183-191. <https://dx.doi.org/10.1016/j.electacta.2016.01.085>
- [20] J.J. Linares, T.A. Rocha, S. Zignani, V.A. Paganin, E.R. Gonzalez, Different anode catalyst for high temperature polybenzimidazole-based direct ethanol fuel cells, *Int. J. Hydrogen Energy* 38 (2013) 620-630. <http://dx.doi.org/10.1016/j.ijhydene.2012.06.113>
- [21] N. Nakagawa, Y. Kaneda, M. Wagatsuma, T. Tsujiguchi, Product distribution and the reaction kinetics at the anode of direct ethanol fuel cell with Pt/C, PtRu/C and PtRuRh/C, *J. Power Sources* 199 (2012) 103–109. <https://doi.org/10.1016/j.jpowsour.2011.10.057>
- [22] F. Zhu, K. Tu, L. Huang, X. Qu, J. Zhang, H. Liao, Z. Zhou, Y. Jiang, S. Sun, High selectivity PtRh/RGO catalysts for ethanol electro-oxidation at low potentials: enhancing the efficiency of CO₂ from alcoholic groups, *Electrochim. Acta* 292 (2018) 2018–216. <https://doi.org/10.1016/j.electacta.2018.08.142>

- [23] M.A.F. Akhairy, S.K. Kamarudin, Catalysts in direct ethanol fuel cell (DEFC): an overview, *Int. J. Hydrogen Energy* 41 (2016) 4214–4228. <https://doi.org/10.1016/j.ijhydene.2015.12.145>
- [24] E. Antolini, Catalysts for direct ethanol fuel cells, *J. Power Sources* 170 (2007) 1–12. <https://doi.org/10.1016/j.jpowsour.2007.04.009>
- [25] F.C. Simões, D.M. dos Anjos, F. Vigier, J.-M. Léger, F. Hahn, C. Coutanceau, E.R. Gonzalez, G. Tremiliosi-Filho, A.R. de Andrade, P. Olivi, K.B. Kokoh, Electroactivity of tin modified platinum electrodes for ethanol electrooxidation, *J. Power Sources* 167 (2007) 1–10. <https://doi.org/10.1016/j.jpowsour.2006.12.113>
- [26] Q. Wang, G.Q. Sun, L.H. Jiang, Q. Xin, S.G. Sun, Y.X. Jiang, S.P. Chen, Z. Jusys, R.J. Behm, Adsorption and oxidation of ethanol on colloid-based Pt/C, PtRu/C and Pt₃Sn/C catalysts: in situ FTIR spectroscopy and on-line DEMS studies, *Phys. Chem. Chem. Phys.* 9 (2007) 2686–2696. <https://doi.org/10.1039/B700676B>
- [27] Y. Wang, S. Song, G. Andreadis, H. Liu, P. Tsiakaras, Understanding the electro-oxidative activity of PtSn in direct ethanol fuel cells, *J. Power Sources* 196 (2011) 4980–4986. <https://doi.org/10.1016/j.jpowsour.2011.01.069>
- [28] S.C. Zignani, V. Baglio, J.J. Linares, G. Monforte, E.R. González, A.S. Aricò, Endurance study of a solid polymer electrolyte direct ethanol fuel cell based on a Pt-Sn anode catalyst, *Int. J. Hydrogen Energy* 38 (2013) 11576–11582. <https://doi.org/10.1016/j.ijhydene.2013.04.162>
- [29] Y. Zhou, Q. Xu, A review of Pt-based anode catalysts preparation for direct ethanol fuel cell, *Advanced Materials Research* 860-863 (2014) 797–800. <https://doi.org/10.4028/www.scientific.net/AMR.860-863.797>
- [30] J. Asgardí, J.C. Calderón, F. Alcaide, A. Querejeta, L. Calvillo, M.J. Lázaro, G. García, E. Pastor, Carbon monoxide and ethanol oxidation on PtSn supported

catalysts: effect of the nature of the carbon support and Pt:Sn composition, *Appl. Catal. B: Env.* 168-169 (2015) 33–41. <https://doi.org/10.1016/j.apcatb.2014.12.003>

[31] F.E. Lopez-Suarez, C.T. Carvalho-Filho, A. Bueno-Lopez, J. Arboleda, A. Echavarria, K.I.B. Eguiluz, G.R. Salazar-Banda, Platinum-tin/carbon catalysts for ethanol oxidation: influence of Sn content on the electroactivity and structural characteristics, *Int. J. Hydrogen Energy* 40 (2015) 12674–12686. <https://doi.org/10.1016/j.ijhydene.2015.07.135>

[32] H. Gharibi, S. Sadeghi, F. Golmohammadi, Electrooxidation of ethanol on highly active and stable carbon supported PtSnO₂ and its application in passive direct ethanol fuel cell: effect of tin oxide synthesis method, *Electrochim. Acta* 190 (2016) 1100–1112. <https://doi.org/10.1016/j.electacta.2015.12.208>

[33] K. Miecznikowski, P.J. Kulesza, Activation of dispersed PtSn/C nanoparticles by tungsten oxide matrix towards more efficient oxidation of ethanol, *J. Power Sources* 196 (2011) 2595–2601. <https://doi.org/10.1016/j.jpowsour.2010.10.078>

[34] V.P. Santos, G. Tremiliosi-Filho, Effect of osmium coverage on platinum single crystals in the ethanol electrooxidation, *J. Electroanal. Chem.* 554–555 (2003) 395–405. [https://doi.org/10.1016/S0022-0728\(03\)00311-5](https://doi.org/10.1016/S0022-0728(03)00311-5)

[35] M.C. Figueiredo, A. Santasalo-Aarnio, F.J. Vidal-Iglesias, J. Solla-Gullón, J.M. Feliu, K. Kontturi, T. Kallio, Tailoring properties of platinum supported catalysts by irreversible adsorbed adatoms toward ethanol oxidation for direct ethanol fuel cells, *Appl. Catal. B: Environ.* 378 (2013) 140–141. <https://doi.org/10.1016/j.apcatb.2013.04.038>

[36] Y. H. Chu, Y. G. Shul, Combinatorial investigation of Pt-Ru-Sn alloys as an anode electrocatalysts for direct alcohol fuel cells, *Int. J. Hydrogen Energy* 35 (2010) 11261–11270. <https://doi.org/10.1016/j.ijhydene.2010.07.062>

- [37] S. Beyhan, J.-M. Léger, F. Kadirgan, Pronounced synergetic effect of the nano-sized PtSnNi/C catalyst for ethanol oxidation in direct ethanol fuel cell, *Appl. Catal. B: Environ.* 130-131 (2013) 305–313. <https://doi.org/10.1016/j.apcatb.2012.11.007>
- [38] S. Beyhan, C. Coutanceau, J.-M. Léger, T.W. Napporn, F. Kadirgan, Promising anode candidates for direct ethanol fuel cell: carbon supported PtSn-based trimetallic catalysts prepared by bönnemann method, *Int. J. Hydrogen Energy* 38 (2013) 6830–6841. <https://doi.org/10.1016/j.ijhydene.2013.03.058>
- [39] J.-M. Jin, T. Sheng, X. Lin, R. Kavanagh, P. Hamer, P. Hu, C. Hardacre, A. Martinez-Bonastre, J. Sharman, D. Thompsett, W.-F. Lin, the origin of high activity but low CO₂ selectivity on binary PtSn in the direct ethanol fuel cell, *Phys. Chem. Chem. Phys.* 16 (2014) 9432–9440. <https://doi.org/10.1039/C4CP00859F>
- [40] J.P.I. de Souza, S.L. Queiroz, K. Bergamaski, E.R. Gonzalez, F.C. Nart, Electro-oxidation of ethanol on Pt, Rh, and PtRh electrodes. A study using DEMS and in-situ FTIR techniques, *J. Phys. Chem. B* 106 (2002) 9825–9830. <https://doi.org/10.1021/jp014645c>
- [41] F.H.B. Lima, D. Profeti, W.H. Lizcano-Valbuena, E.A. Ticianelli, E.R. Gonzalez, Carbon-dispersed Pt–Rh nanoparticles for ethanol electro-oxidation. Effect of the crystallite Size and of temperature, *J. Electroanal. Chem* 617 (2008) 121–129. <https://doi.org/10.1016/j.jelechem.2008.01.024>
- [43] K. Bergamaski, E.R. Gonzalez, F.C. Nart, Ethanol oxidation on carbon supported platinum-rhodium bimetallic catalysts, *Electrochim. Acta* 53 (2008) 4396–4406. <https://doi.org/10.1016/j.electacta.2008.01.060>
- [43] L. Rao, Y.-X. Jiang, B.-W. Zhang, Y.-R. Cai, S.-G. Sun, High activity of cubic PtRh alloys supported on graphene towards ethanol electrooxidation, *Phys. Chem. Chem. Phys.* 16 (2014) 13662–13671. <https://doi.org/10.1039/C3CP55059A>

- [44] N. Erini, P. Krause, M. Gliech, R. Yang, Y. Huang, P. Strasser, Comparative assessment of synthetic strategies toward active platinum-rhodium-tin electrocatalysts for efficient ethanol electro-oxidation, *J. Power Sources* 294 (2015) 299–304. <https://doi.org/10.1016/j.jpowsour.2015.06.042>
- [45] A.B. Delpeuch, M. Chatenet, M.R. Rau, C. Cremers, Influence of H- and OH- adsorbates on the ethanol oxidation reaction - A DEMS study, *Phys. Chem. Chem. Phys.* 17 (2015) 10881–10893. <https://doi.org/10.1039/C5CP00132C>
- [46] A.L. Soares, C. Morais, T.W. Napporn, B.K. Kokoh, P. Olivi, Beneficial effects of rhodium and tin oxide on carbon supported platinum catalysts for ethanol electrooxidation, *J. Power Sources* 315 (2016) 7–55. <https://doi.org/10.1016/j.jpowsour.2016.03.013>
- [47] Y. Shen, M.Z. Zhang, K. Xiao, J. Xi, Synthesis of Pt, PtRh, and PtRhNi alloys supported by pristine graphene nanosheets for ethanol oxidation, *ChemCatChem* 6 (2014) 3254–3261. <https://doi.org/10.1002/cctc.201402629>
- [48] G. Yang, A.I. Frenkel, D. Su, X. Teng, Enhanced electrokinetics of C-C bond splitting during ethanol oxidation by using a Pt/Rh/Sn catalyst with a partially oxidized Pt and Rh Core and a SnO₂ shell, *ChemCatChem* 8 (2016) 2876–2880. <https://doi.org/10.1002/cctc.201600429>
- [49] N. Nakagawa, T. Watanabe, M. Wagatsuma, T. Tsujiguchi, Carbon-Supported PtRuRh Nano Particles as a Catalyst for Direct Ethanol Fuel Cells, *Key Eng. Mater.* 497 (2012) 67-72. <http://doi.org/10.4028/www.scientific.net/KEM.497.67>
- [50] W.J. Zhou, W.Z. Li, S.Q. Song, Z.H. Zhou, L.H. Jiang, G.Q. Sun, Q. Xin, K. Poulianitis, S. Kontou, P. Tsiakaras, Bi- and tri-metallic Pt-based anode catalysts for direct ethanol fuel cells, *J. Power Sources* 131 (2004) 217-223. <https://doi.org/10.1016/j.jpowsour.2003.12.040>

- [51] W.J. Zhou, B. Zhou, W.Z. Li, Z.H. Zhou, S.Q. Song, G.Q. Sun, Q. Xin, S. Douvartzides, M. Goula, P. Tsiakaras, Performance comparison of low-temperature direct alcohol fuel cells with different anode catalysts, *J. Power Sources* 126 (2004) 16-22. <https://doi.org/10.1016/j.jpowsour.2003.08.009>
- [52] E.V. Spinacé, R.R.Dias, M. Brandalise, M. Linardi, A.O. Neto, Electro-oxidation of ethanol using PtSnRh/C electrocatalysts prepared by an alcohol-reduction process, *Ionics* 16 (2010) 91-95. <https://doi.org/10.1007/s11581-009-0396-3>
- [53] M.K. Rashed, M.A.I.N. Salleh, H.A. Abdul Bari, M.H.S. Ismail, S. Izhar, The effects of electrode and catalyst selection on microfluidic fuel cell performance, *ChemBioEng. Rev.* 2 (2015) 356–372. <https://doi.org/10.1002/cben.201500007>
- [54] G. Gautier, S. Kouassi, Integration of porous silicon in micro fuel cells: a review, *Int. J. Energy Res.* 39 (2015) 1–25. <https://doi.org/10.1002/er.3206>
- [55] F. Alcaide, O. Miguel, H.-J Grande, New approach to prepare Pt-based hydrogen diffusion anodes tolerant to CO for polymer electrolyte membrane fuel cells, *Catal. Today* 116 (2006) 408–414. <https://doi.org/10.1016/j.cattod.2006.05.077>
- [56] B. Oleg, M. Sarrazin, D. Belanger, L. Roue, Rhodium deposits on pyrolytic graphite: physico-chemical properties and electrocatalytic activity towards nitrate reduction in neutral medium, *Appl. Catal. B: Env.* 63 (2006) 243–253. <https://doi.org/10.1016/j.apcatb.2005.11.016>
- [57] I.A. Rodrigues, K. Bergamaski, F.C. Nart, Probing n-propanol electrochemical oxidation on bimetallic PtRh codeposited electrodes, *J. Electrochem. Soc.* 150 (2003) E89–E94. <https://doi.org/10.1149/1.1532327>
- [58] W. Tokarz, H. Siwek, P. Piela, A. Czerwiński, Electro-oxidation of methanol on Pt-Rh alloys, *Electrochim. Acta* 52 (2007) 5565–5573. <https://doi.org/10.1016/j.electacta.2006.12.016>

- [59] S.S. Gupta, J. Datta, A comparative study on ethanol oxidation behavior at Pt and PtRh electrodeposits, *J. Electroanal. Chem.* 594 (2006) 65–72. <https://doi.org/10.1016/j.jelechem.2006.05.022>
- [60] D. Pletcher, R.I. Urbina, Electrodeposition of rhodium. Part 2. Sulfate solutions, *J. Electroanal. Chem.* 421 (1997) 145–151. [https://doi.org/10.1016/S0022-0728\(96\)04845-0](https://doi.org/10.1016/S0022-0728(96)04845-0)
- [61] E.P. Leão, M.J. Giz, G.A. Camara, G. Maia, Rhodium in presence of platinum as a facilitator of carbon-carbon bond break: a composition study, *Electrochim. Acta* 56 (2011) 1337–1343. <https://doi.org/10.1016/j.electacta.2010.10.006>
- [62] J.P. Iúdice de Souza, T. Iwasita, F.C. Nart, W. Vielstic, Performance evaluation of porous electrocatalysts via normalization of the active surface, *J. Appl. Electrochem.* 30 (2000) 43–48. <https://doi.org/10.1023/A:1003896604569>
- [63] F. Alcaide, G. Álvarez, J.A. Blazquez, P.L. Cabot, O. Miguel, Development of a novel portable-size PEMFC short stack with electrodeposited Pt hydrogen diffusion anodes, *Int. J. Hydrogen Energy* 35 (2010) 5521–5527. <https://doi.org/10.1016/j.ijhydene.2010.03.012>
- [64] L. Fang, F.J. Vidal-Iglesias, S.E. Huxter, G.A. Attard, P.B. Wells, RhPt/graphite catalysts for CO electrooxidation: performance of mixed metal and alloyed surfaces, *Surf. Sci.* 631 (2015) 258–266. <https://doi.org/10.1016/j.susc.2014.06.026>
- [65] C.J. Corcoran, H. Tavassol, M.A. Rigsby, P.S. Bagus, A. Wieckowski, Application of XPS to study electrocatalysts for fuel cells, *J. Power Sources* 195 (2010) 7856–7879. <https://doi.org/10.1016/j.jpowsour.2010.06.018>
- [66] M.A. Rigsby, W.P. Zhou, A. Lewera, H.T. Duong, P.S. Bagus, W. Jaegermann, R. Hunger, A. Wieckowski, Experiment and theory of fuel cell catalysis: methanol and

- formic acid decomposition on nanoparticle Pt/Ru, *J. Phys. Chem. C* 112 (2008) 15595–15601. <https://doi.org/10.1021/jp805374p>
- [67] H. Angerstein-Kozłowska, in: E. Yeager, J.O'M. Bockris, B.E. Conway, S. Sarangapani (Eds.), *Comprehensive Treatise of Electrochemistry*, Springer US: Plenum Press, New York, 1984, Vol. 9, p. 15–59.
- [68] E. Antolini, Effect of the structural characteristics of binary Pt-Ru and ternary Pt-Ru-M fuel cell catalysts on the activity of ethanol electrooxidation in acid medium, *ChemSusChem* 6 (2013) 966–973. <https://doi.org/10.1002/cssc.201300138>
- [69] A. Ruban, B. Hammer, P. Stoltze, H.L. Skriver, J.K. Nørskov, Surface electronic structure and reactivity of transition and noble metals, *J. Mol. Catal. A-Chem.* 115 (1997) 421–429. [https://doi.org/10.1016/S1381-1169\(96\)00348-2](https://doi.org/10.1016/S1381-1169(96)00348-2)
- [70] D.B. Šepa, in: B.E. Conway, R.E. White, J.O'M. Bockris, (Eds.), *Modern Aspects of Electrochemistry*, Plenum Press, New York, 1996, No. 129, pp. 1–56.
- [71] A.B. Delpuech, T. Asset, M. Chatenet, C. Cremers, Influence of the temperature for the ethanol oxidation reaction (EOR) on Pt/C, PtRh/C and Pt-Rh-SnO₂, *Fuel Cells* 15 (2015) 352–360. <https://doi.org/10.1002/fuce.201400144>
- [72] V. Rao, C. Cremers, U. Stimming, L. Cao, S. Sun, S. Yan, G. Sun, Q. Xin, Electro-oxidation of ethanol at gas diffusion electrodes a DEMS study, *J. Electrochem. Soc.* 154 (2007) B1138–B1147. <https://doi.org/10.1149/1.2777108>

Figure captions

Fig. 1.- Selected FE-SEM images of the microporous carbon layer after the electrodeposition of the (a) Pt, (b) Pt₈₀Rh₂₀, (c) Pt₆₀Rh₄₀, and (d) Rh (magnification 75 kX).

Fig. 2.- XRD diffractograms corresponding to the PtRh catalysts with different atomic ratio: (a) Pt, (b) Pt₈₀Rh₂₀, (c) Pt₆₀Rh₄₀, and (d) Rh. The diffractogram of the supporting carbon paper is also depicted for comparison. In parentheses the planes corresponding to characteristic diffraction signals of FCC Pt (diamonds) and Rh (circles).

Fig. 3.- XPS spectra corresponding to Pt 4f and Rh 3d regions of the surface of the PtRh catalysts (a) Pt; (b) Rh; (c) and (d) Pt₈₀Rh₂₀; and (e) and (f) Pt₆₀Rh₄₀.

Fig. 4.- Cyclic voltammograms of the (a) Pt, (b) Pt₈₀Rh₂₀, (c) Pt₆₀Rh₄₀ and (d) Rh electrodeposited electrodes in deaerated 0.50 mol dm⁻³ H₂SO₄ at 20 mV s⁻¹ and 25.0 °C.

Fig. 5.- CO stripping voltammograms of (a) Pt, (b) Pt₈₀Rh₂₀, (c) Pt₆₀Rh₄₀, and (d) Rh in 0.5 mol dm⁻³ H₂SO₄ at 20 mV s⁻¹ and 25.0 °C. Only the first cycles are shown.

Fig. 6.- Cyclic voltammograms for the ethanol oxidation on (a) Pt, (b) Pt₈₀Rh₂₀, (c) Pt₆₀Rh₄₀, and (d) Rh electrodeposited electrodes in 2 mol dm⁻³ ethanol + 0.5 mol dm⁻³ H₂SO₄ at 20 mV s⁻¹ and 60 °C.

Fig. 7.- Linear sweep voltammograms for the ethanol oxidation on (a) Pt, (b) Pt₈₀Rh₂₀, (c) Pt₆₀Rh₄₀, and (d) Rh catalyzed electrodes in 2 mol dm⁻³ ethanol + 0.5 mol dm⁻³ H₂SO₄ at 1.0 mV s⁻¹ and 60 °C. Currents normalized to the corresponding CO stripping charge.

Fig. 8.- (a) Linear sweep voltammograms for the ethanol oxidation on the Pt₆₀Rh₄₀ catalyzed electrode at (a) 70 (b) 60, (c) 40, and (d) 20 °C at 1.0 mV s⁻¹ in 2 mol dm⁻³ ethanol + 0.5 mol dm⁻³ H₂SO₄ and (b) Arrhenius-type plots for the ethanol oxidation on (a) Pt₆₀Rh₄₀, (b) Pt₈₀Rh₂₀, (c) Pt, and (d) Rh catalyzed electrodes in the same solution.

Fig. 9.- Chronoamperograms corresponding to the ethanol oxidation in 2 mol dm^{-3} ethanol + $0.5 \text{ mol dm}^{-3} \text{ H}_2\text{SO}_4$ on (a) Pt, (b) Pt₈₀Rh₂₀, (c) Pt₆₀Rh₄₀, and (d) Rh electrodes at 0.500 V and 60 °C. Currents normalized to the CO stripping charge.

Fig. 10.- Cell voltage (V) and specific power density (P) vs. specific current density curves (I) for the single DEFCs prepared with (a) Pt₆₀Rh₄₀ and (b) Pt₈₀Rh₂₀ anodes. The fuel was 2.0 M ethanol, fed at a flow-rate of 1.5 mL min^{-1} . Humidified pure O₂ at a flow-rate of 50 sccm and atmospheric pressure was fed to the cathode. The cell temperature was 90 °C.

Fig. 11.- Cell voltage (V) and specific power density (P) vs. specific current density curves (I) for the single DEFCs prepared with Pt₆₀Rh₄₀ anodes. The fuel was 2.0 M ethanol, fed at a flow-rate of 1.5 mL min^{-1} . Humidified pure O₂ at a flow-rate of 50 sccm and atmospheric pressure was fed to the cathode. Cell temperatures of (a) 40, (b) 50, (c) 60, (d) 70 and (e) 90 °C.

Table 1.- Properties of some DAFCs at 25 °C and 1 atm as a function of the fuel (M: methanol; E: ethanol; EG: ethyleneglycol). The molecular weight (M_w), electrons involved per mol of the alcohol (n), open circuit voltage (OCV), theoretical energy density (E_{sp}), and capacity of the pure fuel (C) [10,11].

DAFC	Fuel Oxidant	M_w / g mol ⁻¹	n	OCV / V	E_{sp} / Wh kg ⁻¹	C / Ah kg ⁻¹
DMFC	CH ₃ OH O ₂	32.04	6	1.21	6073	5019
DEFC	CH ₃ CH ₂ OH O ₂	46.07	12	1.14	8028	6981
DEGFC	OHCH ₂ CH ₂ OH O ₂	62.07	10	1.22	5268	4318

Table 2.- Maximum power densities (P_{Wm}) and current densities corresponding to P_{Wm} (j_m) in DEFCs built up with the indicted anode catalysts and membranes of Nafion[®] or polybenzimidazole (PBI).

Catalyst	[ethanol] / mol dm ⁻³	Membrane	T / °C	P_{Wm} / mW cm ⁻²	j_m / mA cm ⁻²	Reference
Pt/C	2.0	Nafion [®]	80	2.0	15	[49]
Pt/C	1.0	Nafion [®]	90	11	75	[50,51]
Pt/C	1:2 ^a	PBI	150	14	95	[20]
Pt/C	1:2 ^a	PBI	200	31	160	[20]
PtPd(1:1)/C	1.0	Nafion [®]	90	12	75	[50]
PtRh(50:50)/C	2.0	Nafion [®]	100	12	80	[52]
PtRh(90:10)/C	2.0	Nafion [®]	100	12	80	[52]
PtRh(1:1)/C	1:2 ^a	PBI	150	17	85	[20]
PtRh(1:1)/C	1:2 ^a	PBI	200	35	180	[20]
PtRu(1:1)/C	2.0	Nafion [®]	80	3.5	20	[49]
PtRu(1:1)/C	1.0	Nafion [®]	90	20-28	100-120	[19,50,51]
PtRu(1:1)/C + SnO ₂	1.0	Nafion [®]	90	30	140	[19]
PtRu(1:1)/C	1:2 ^a	PBI	150	23	115	[20]
PtRu(1:1)/C	1:2 ^a	PBI	200	54	270	[20]
PtSn(3:1)/C	1.0	Nafion [®]	70	26	80	[18]
PtSn(9:1)/C	1.0	Nafion [®]	90	28	95	[18]
PtSn(3:1)/C	1.0	Nafion [®]	90	40	125	[18]
PtSn(1:1)/C	1.0	Nafion [®]	90	37-52	120-140	[18,50]
PtSn(1:1)/C	2.0	Nafion [®]	100	35	120	[52]
PtSn(1:1)/C	1:2 ^a	PBI	150	19	95	[20]
PtSn(1:1)/C	1:2 ^a	PBI	200	47	195	[20]
PtRuRh(2:1:1)/C	2.0	Nafion [®]	80	10	55	[49]
PtRuSn(1:1:1)/C	1.0	Nafion [®]	90	38	110	[50]
PtSnRh(50:40:10)/C	2.0	Nafion [®]	100	42	135	[52]

^a Ethanol:water weight ratio.

Table 3.- Nominal and bulk (from EDX) composition together with the experimental (XRD) and theoretical (Vegard's law) lattice parameters (a), and crystallite size (XRD) of the prepared PtRh catalysts.

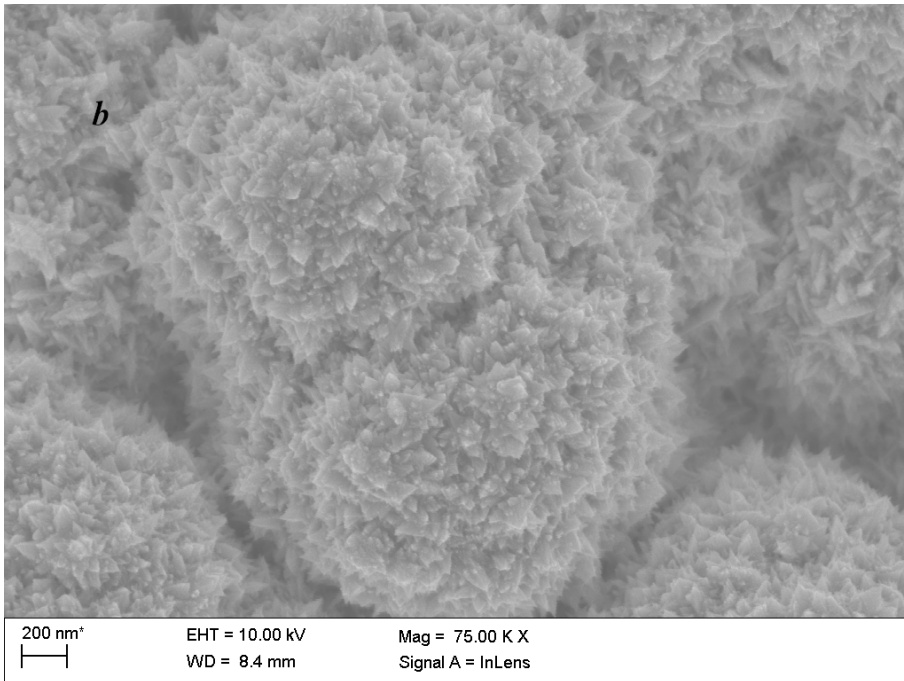
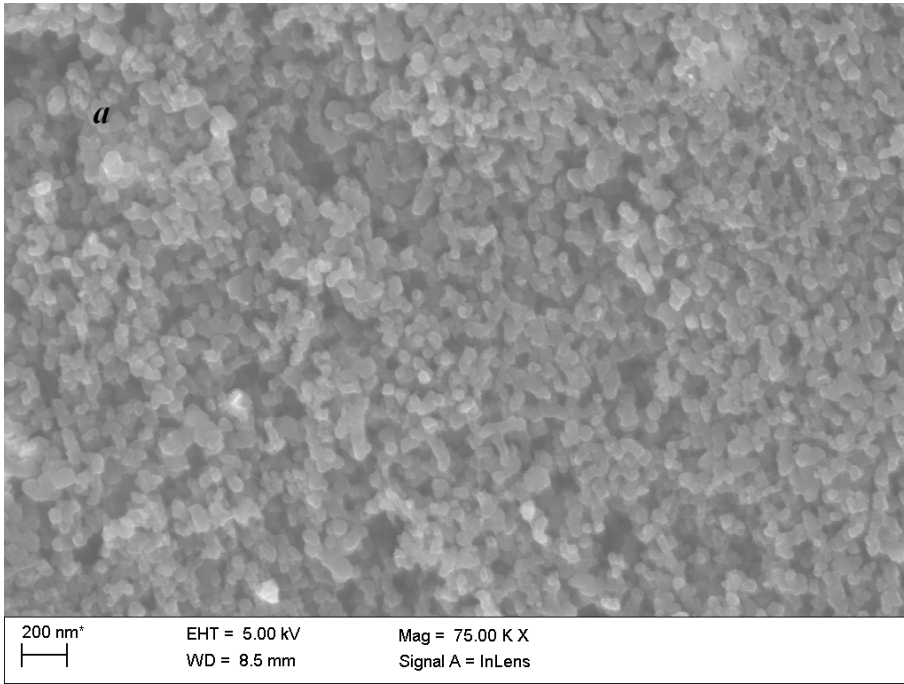
Pt:Rh nominal/at.%	Pt:Rh bulk/at.%	a experimental/nm	a theoretical/nm	Crystallite size/nm
100:0	100:0	0.3910 ± 0.0001	0.3910 ± 0.0001	10.5 ± 0.6
80:20	80.4:19.6	0.3894 ± 0.0004	0.3888 ± 0.0004	8.3 ± 0.5
60:40	62.4:37.6	0.3874 ± 0.0005	0.3868 ± 0.0005	7.0 ± 0.4
0:100	0:100	0.3799 ± 0.0002	0.3799 ± 0.0002	6.1 ± 0.7

Table 4.- XPS compositional results of the electrodeposited PtRh catalysts. The surface composition is compared to the nominal one and the relative atomic percentages of different oxidation states of each element are given.

Pt:Rh nominal/at.%	Pt:Rh surface/at.%	Pt⁰ /at.%	Pt(II) /at.%	Rh⁰ /at.%	Rh(III) /at.%
100:0	100:0	72	28	0	0
80:20	84.7:15.3	61	39	56	44
60:40	62.9:37.1	71	29	55	45
0:100	0:100	0	0	50	50

Table 5.- Onset potentials for the PtRh alloys oxidation (E_{ox}), for CO oxidation from stripping curves at 20 mV s⁻¹ and 25 °C (E_{CO}) and for ethanol oxidation at 1.0 mV s⁻¹ and 60 °C (E_{EtOH}) on the different electrodeposited PtRh catalysts together with the corresponding apparent activation energies for the EOR ($U_{app}^{\#}$).

Pt:Rh	E_{ox}	E_{CO}	E_{EtOH}	$U_{app}^{\#}$
nominal/at.%	/ V	/ V	/ V	/ kJ mol ⁻¹
100:0	0.60	0.69	0.60	51 ± 2
80:20	0.38	0.50	0.46	47 ± 2
60:40	0.36	0.45	0.44	32 ± 2
0:100	0.30	0.59	0.57	76 ± 2



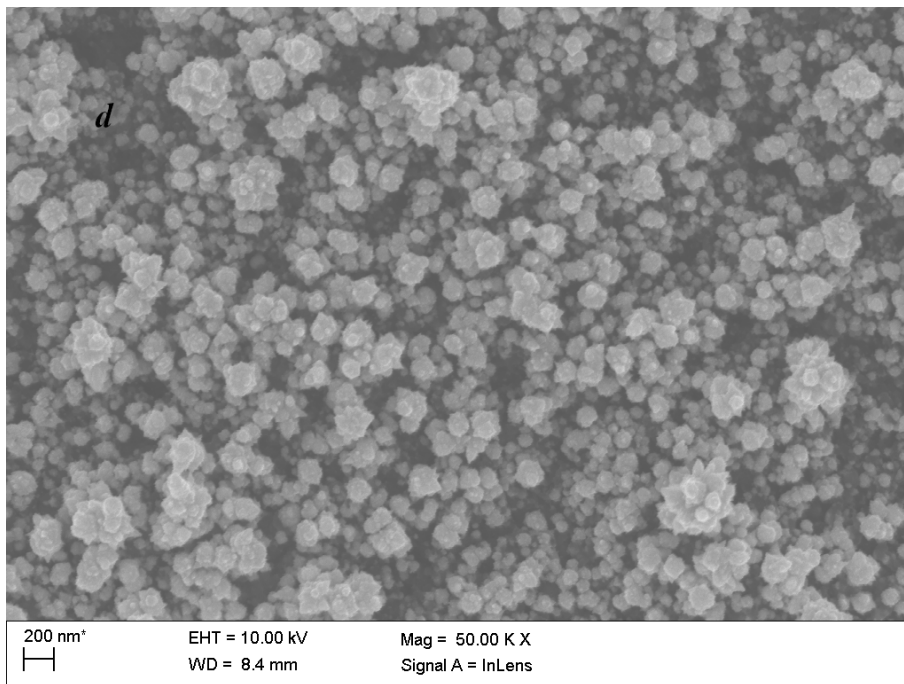
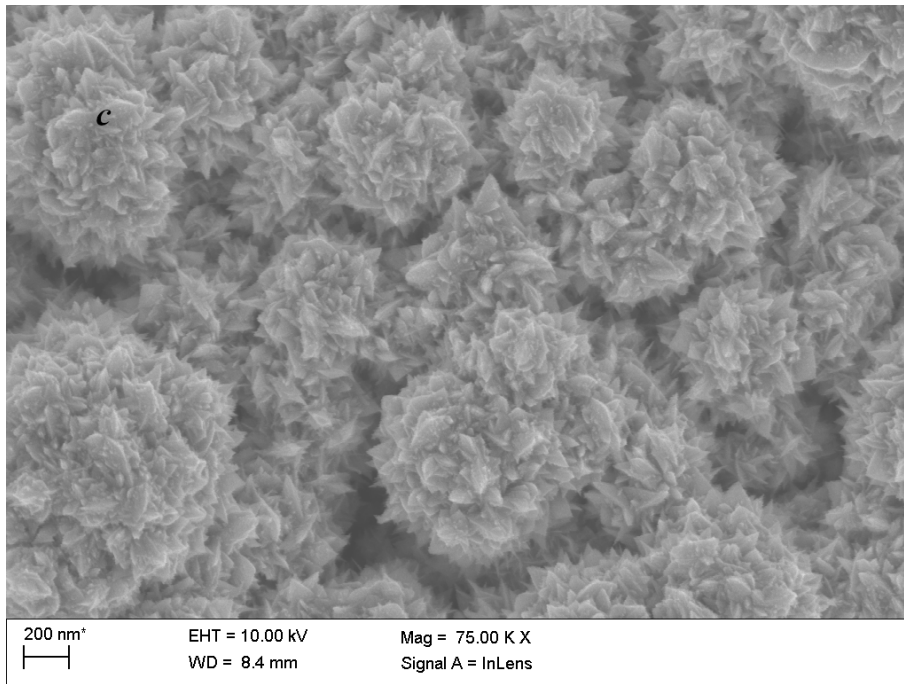


Figure 1

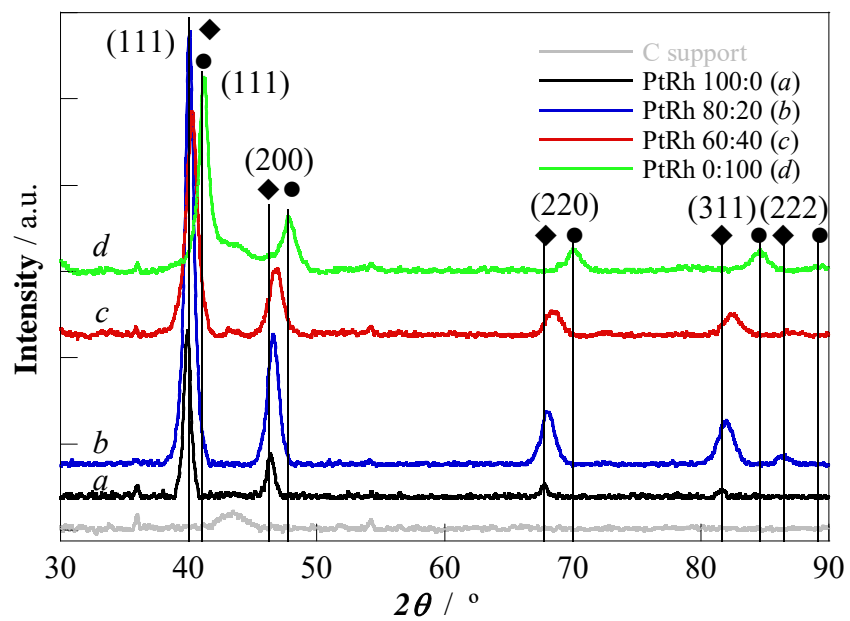
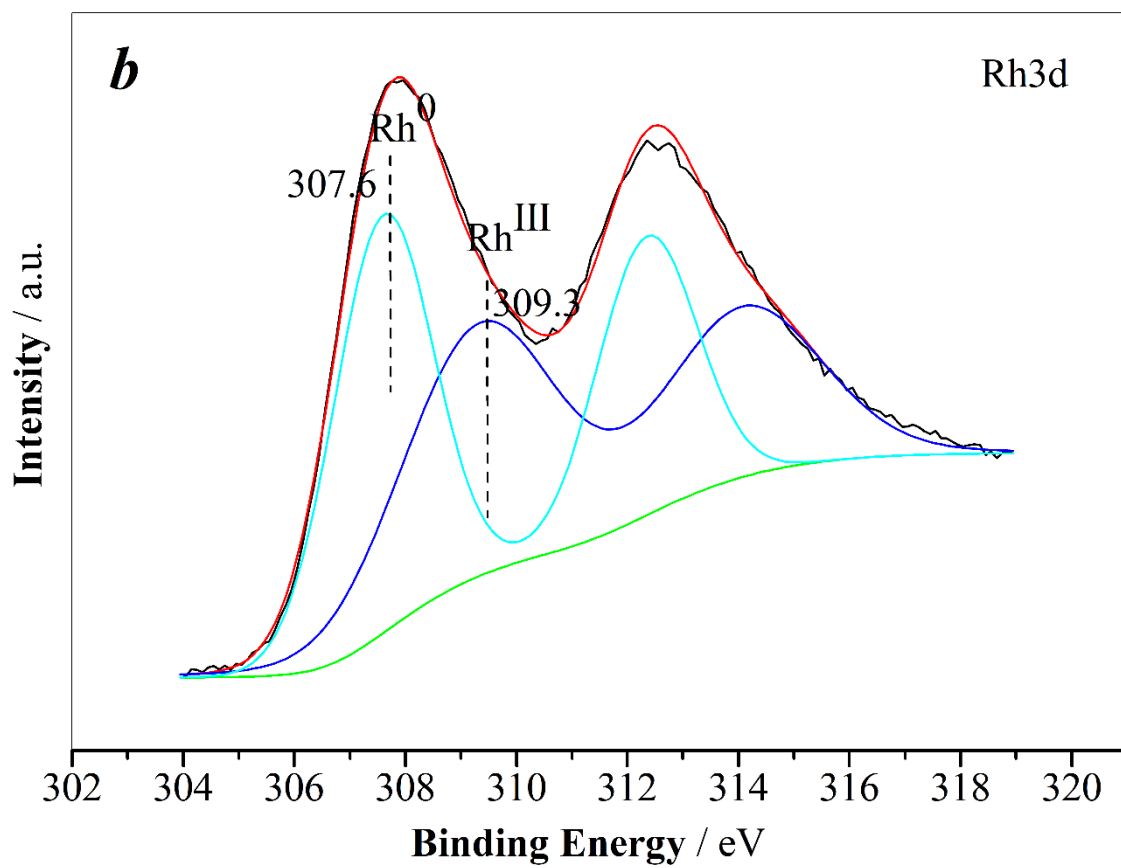
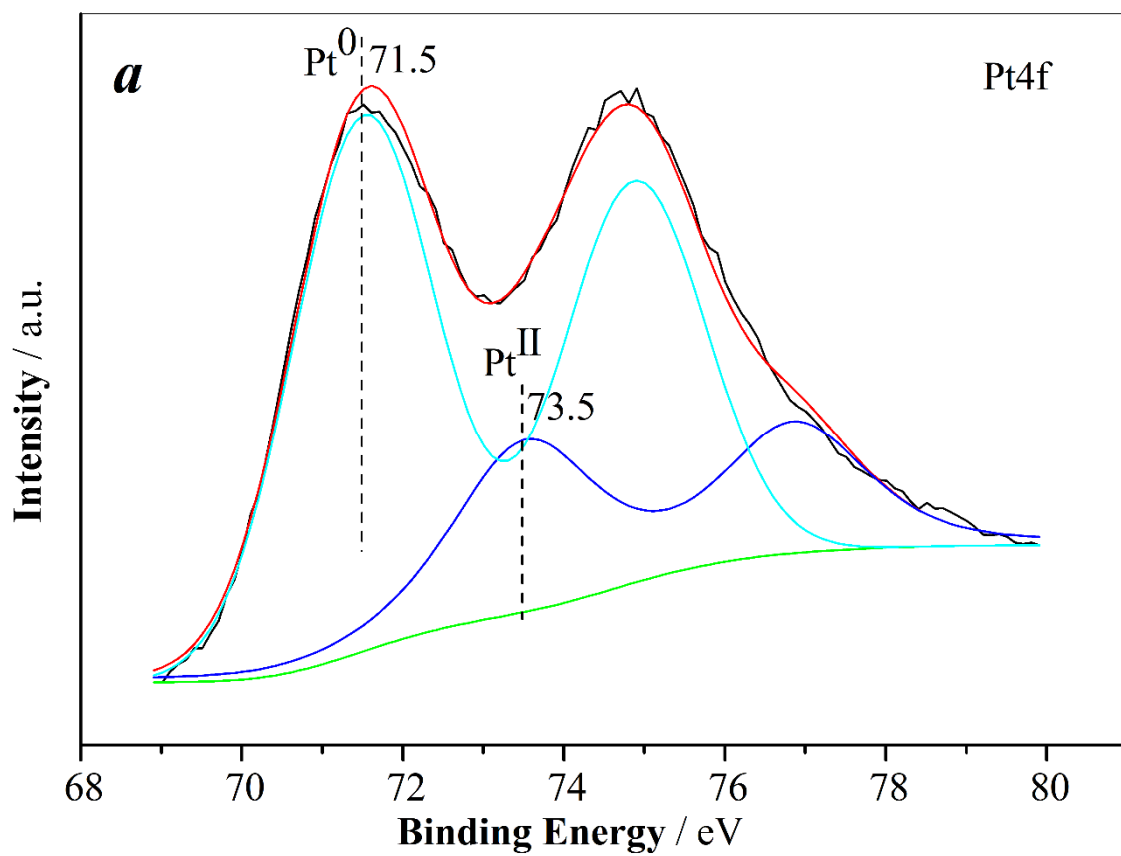
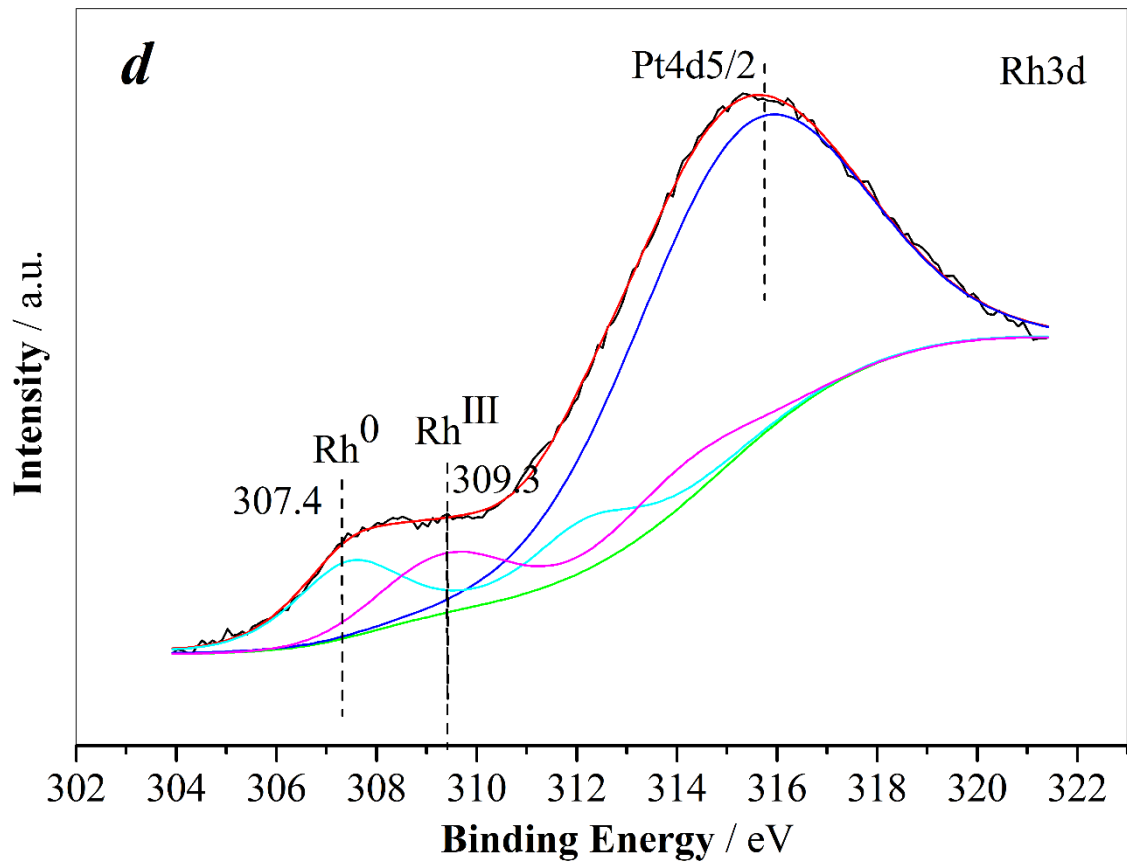
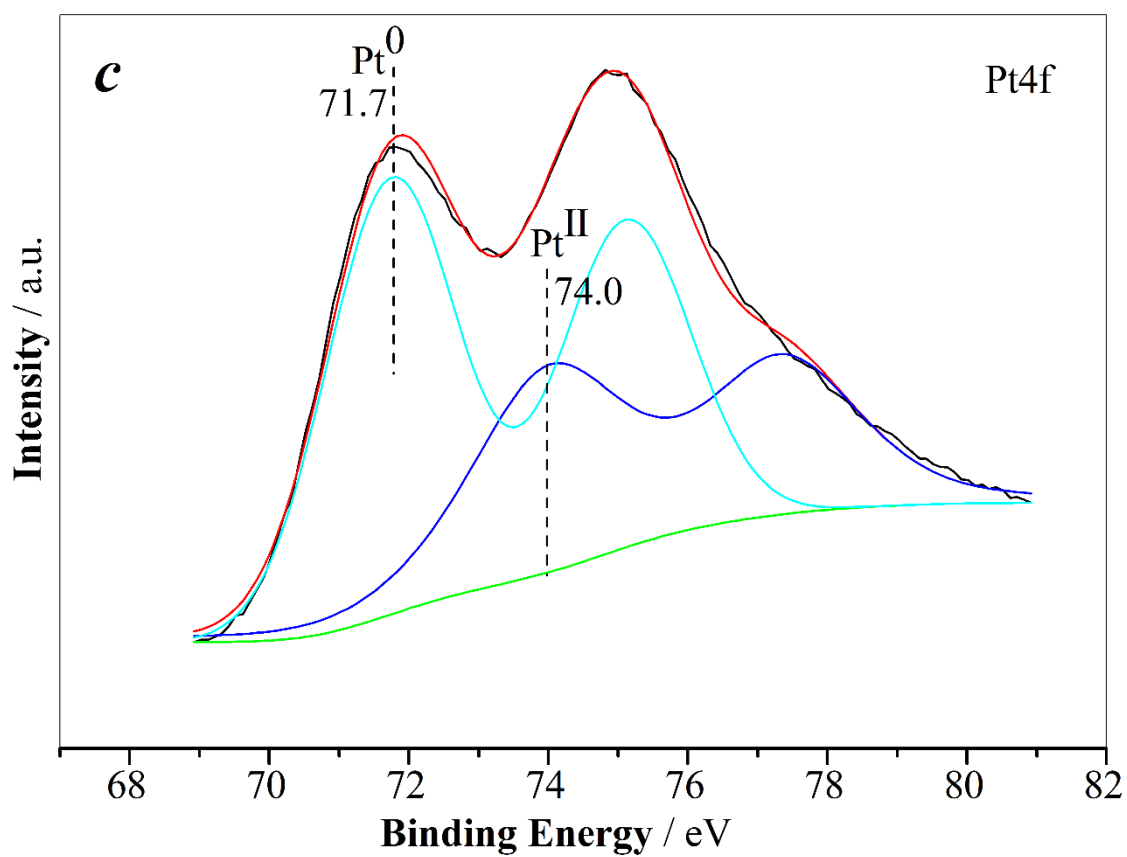


Figure 2





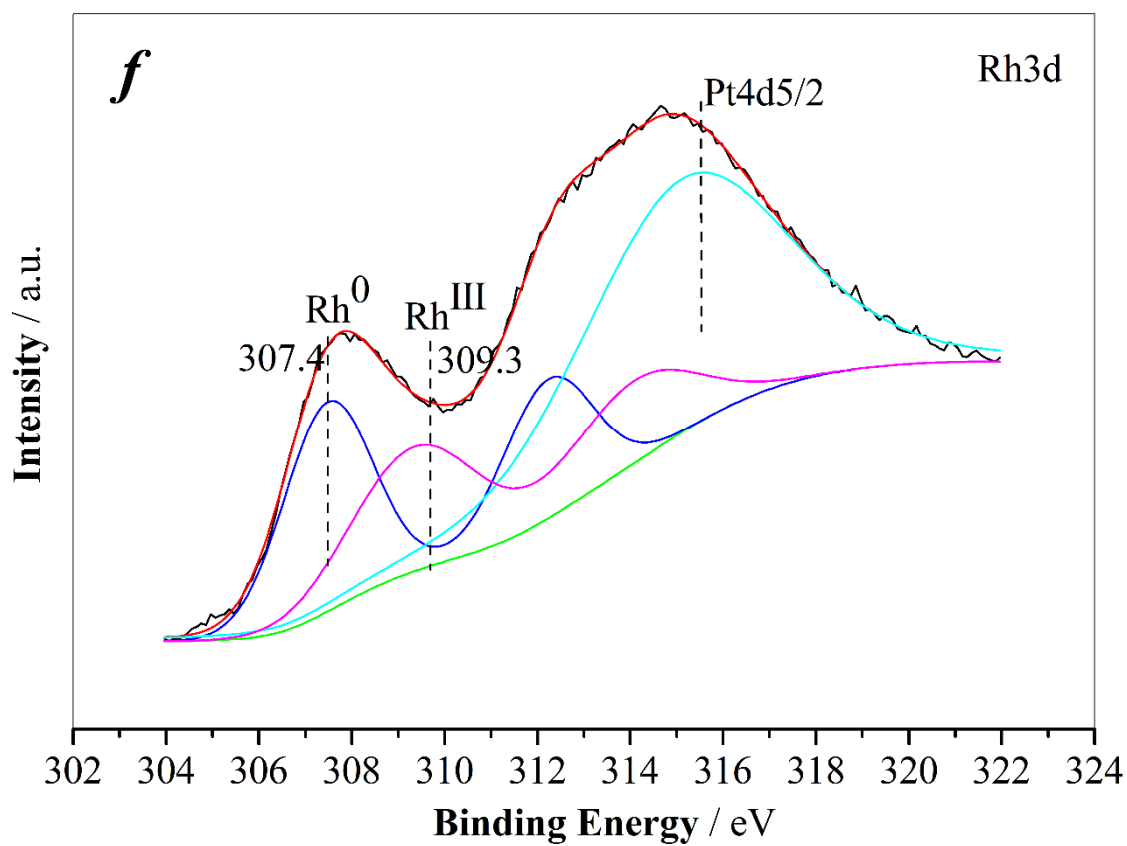
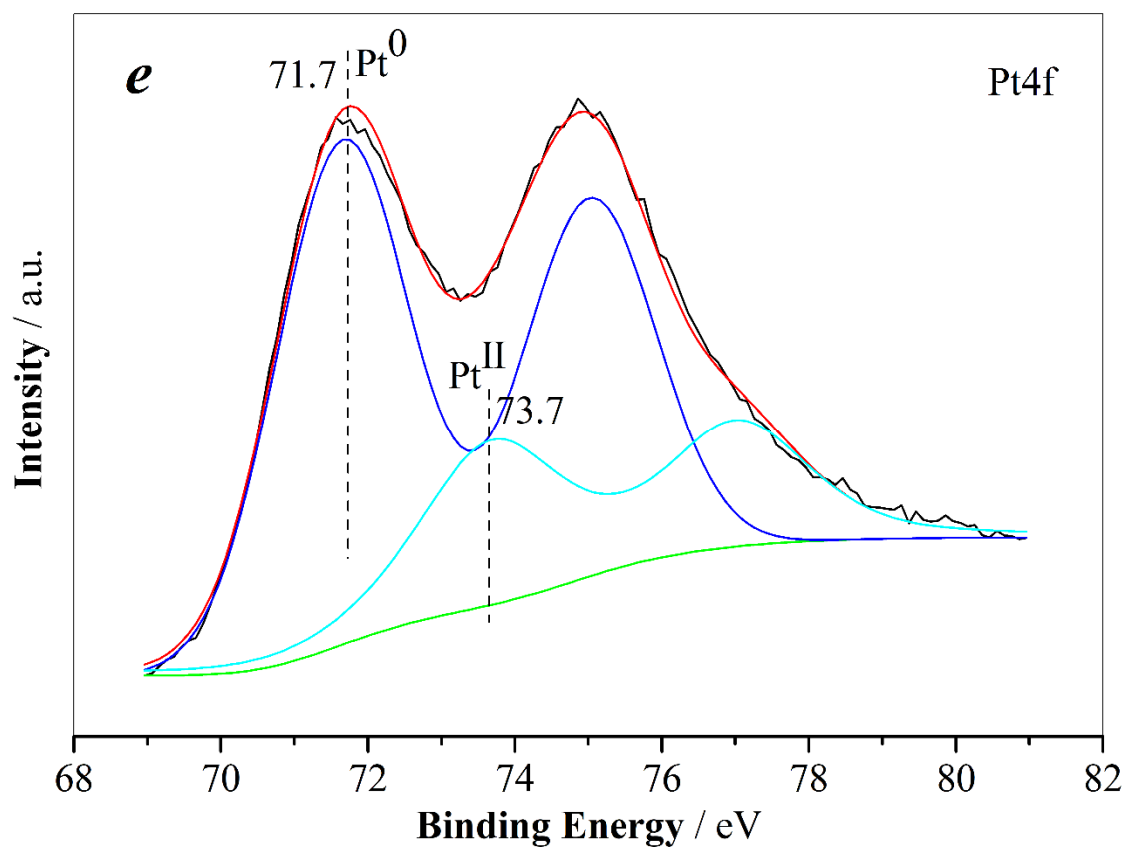


Figure 3

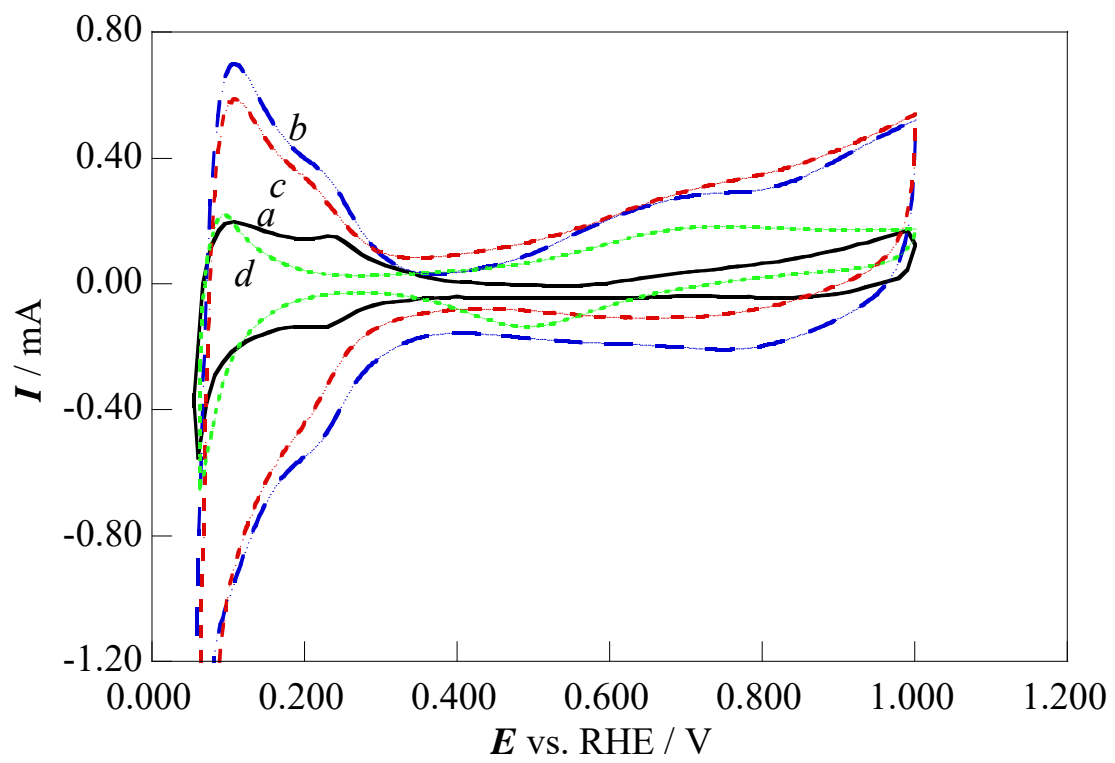


Figure 4

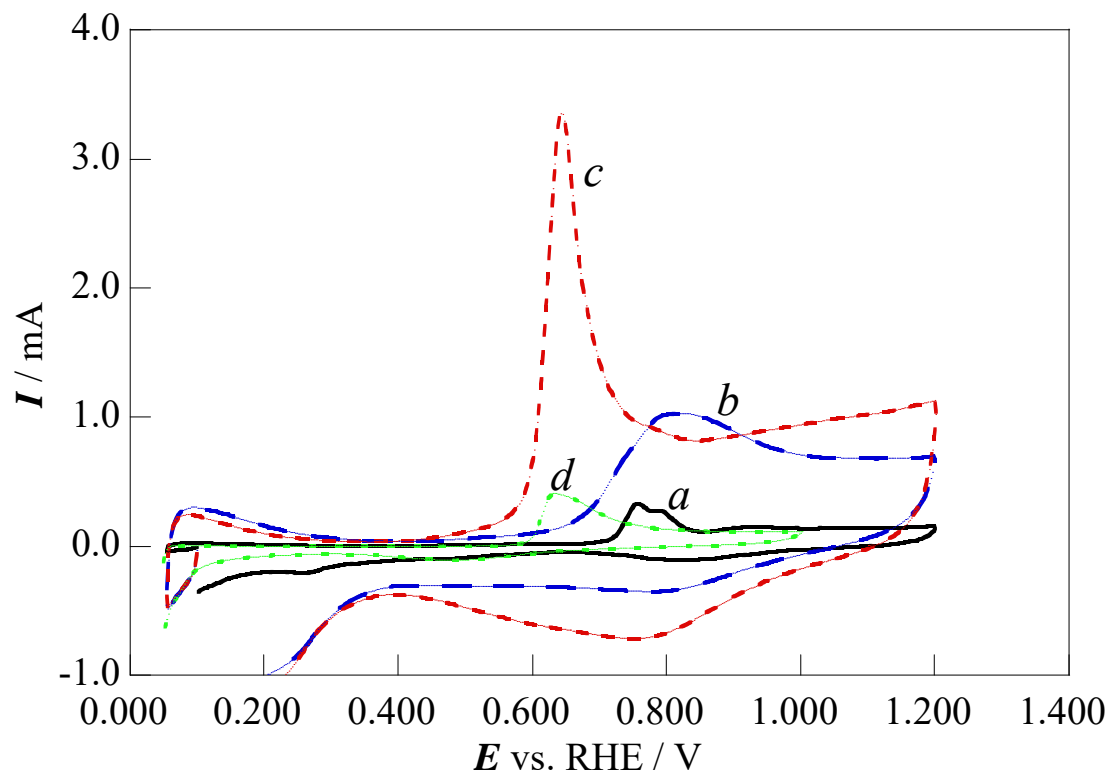


Figure 5

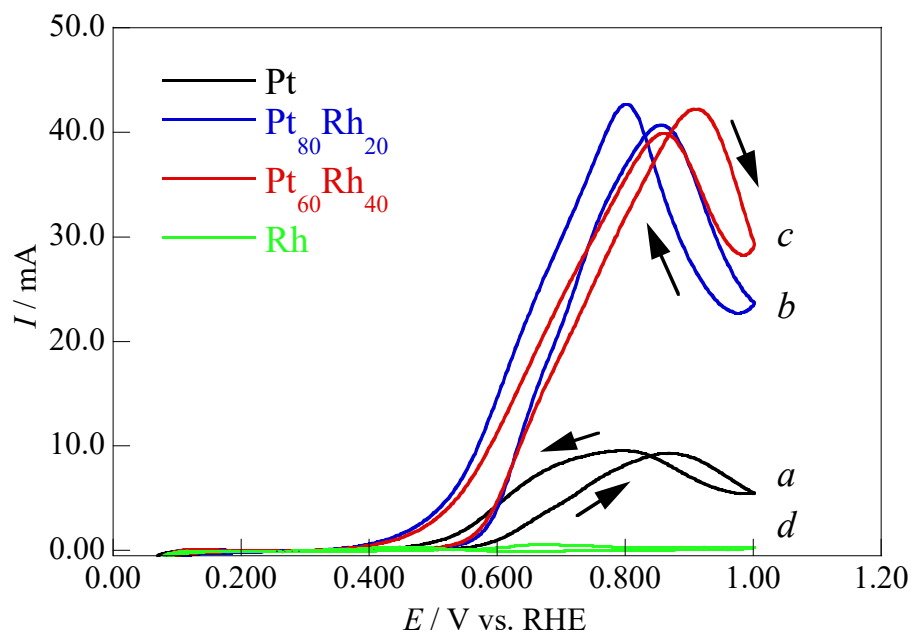


Figure 6

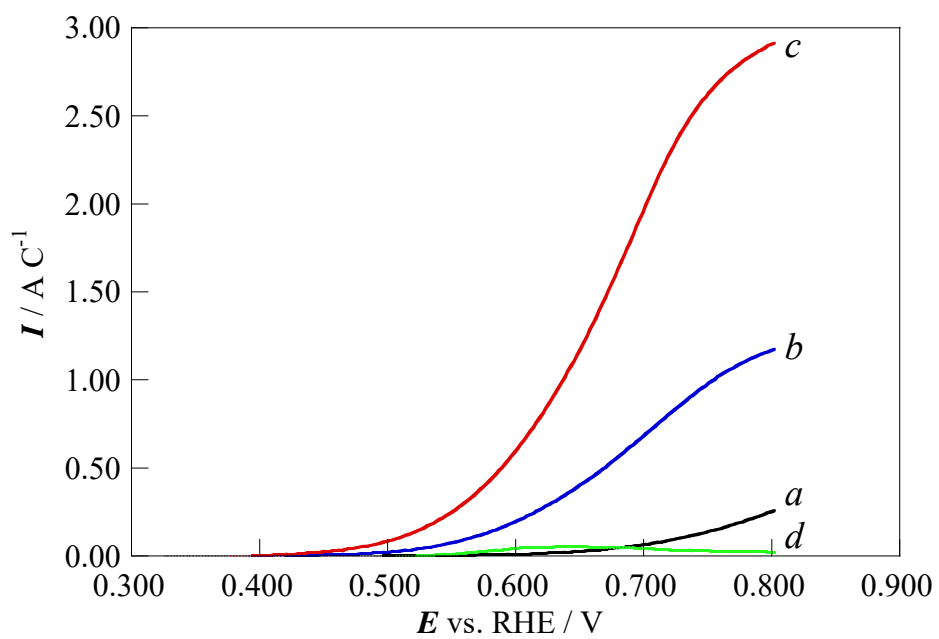


Figure 7

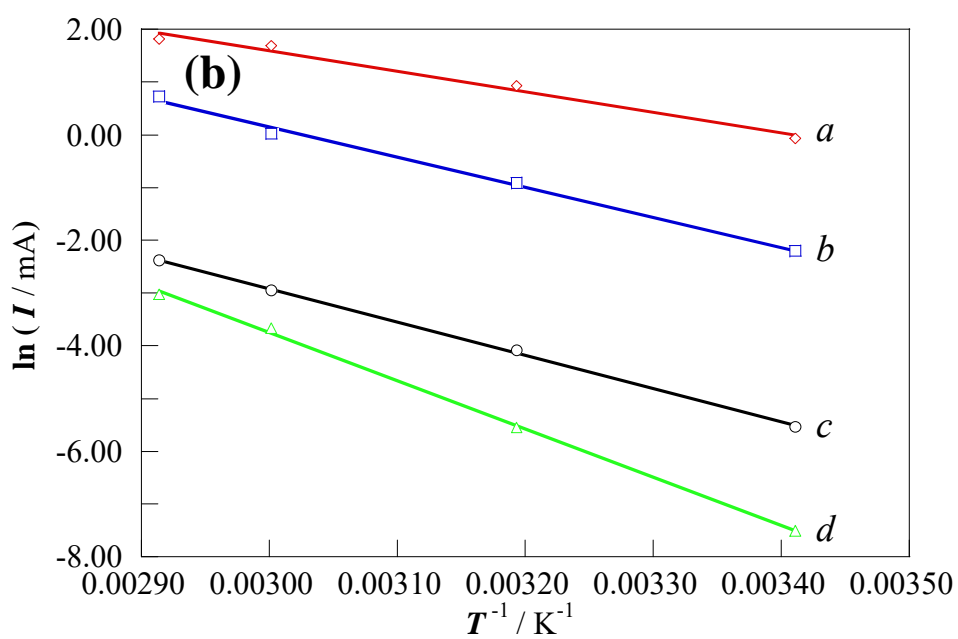
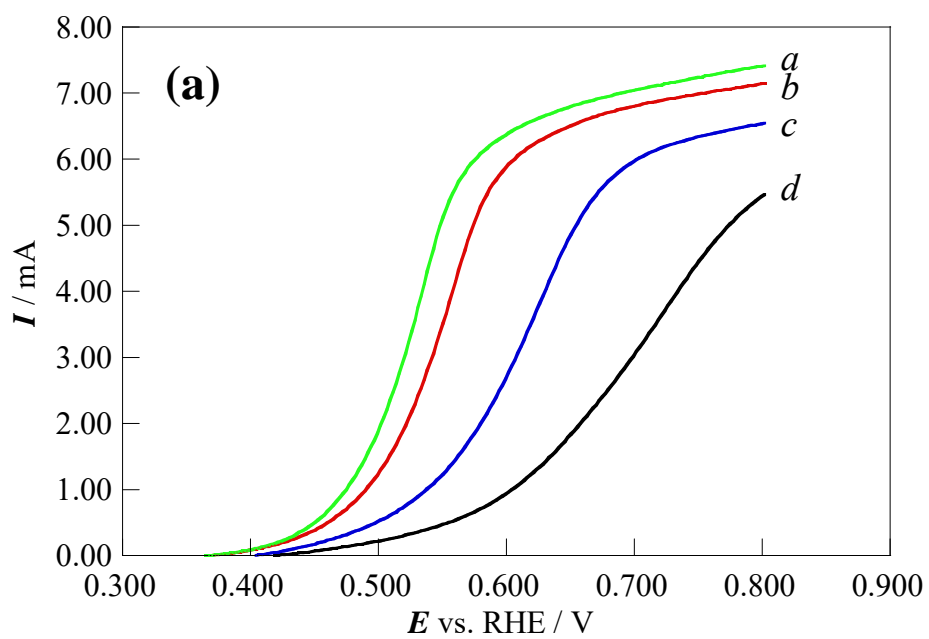


Figure 8

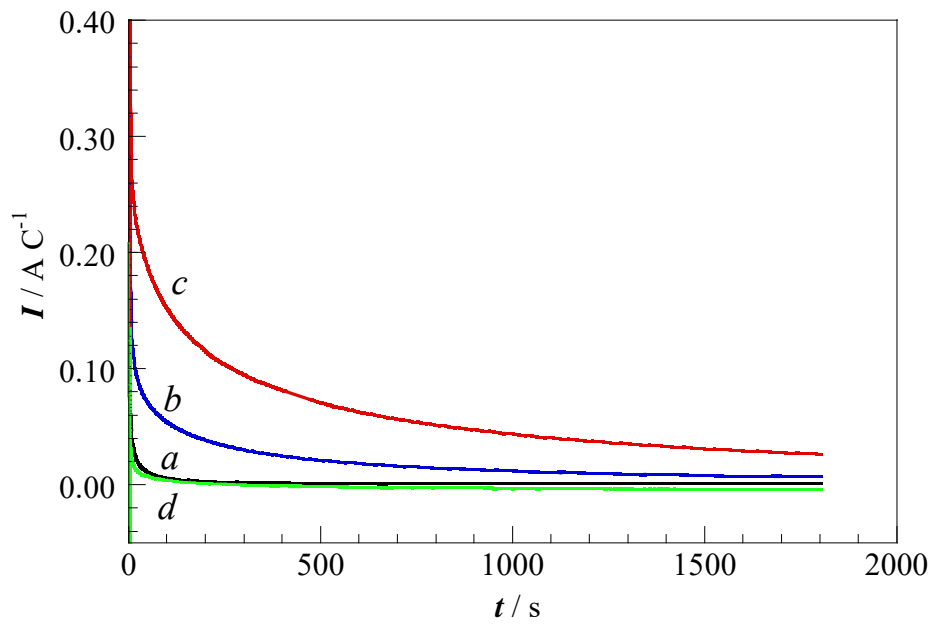


Figure 9

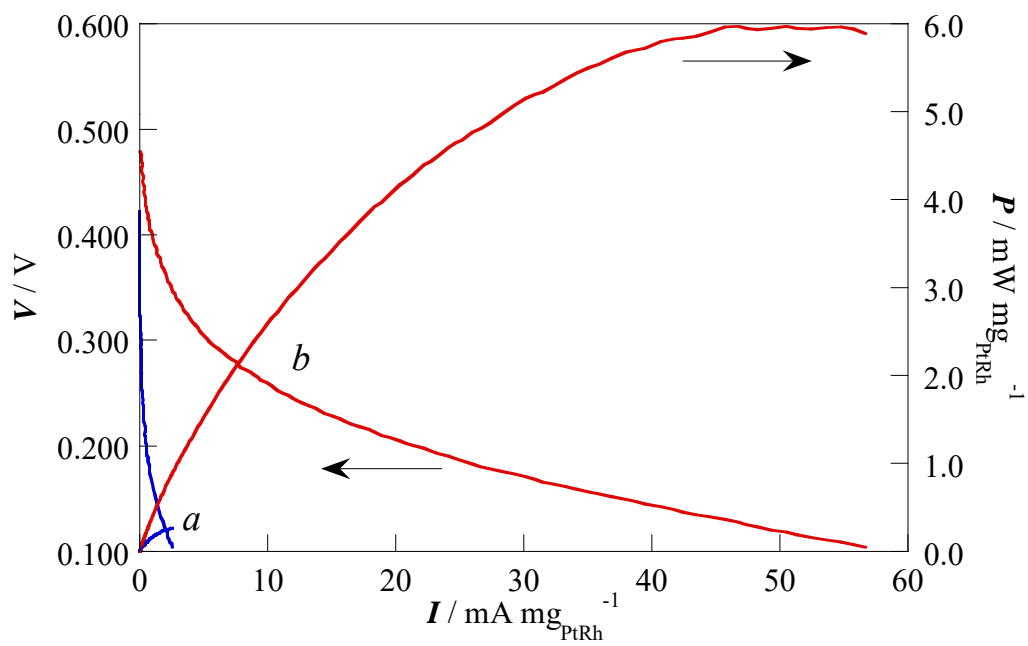


Figure 10

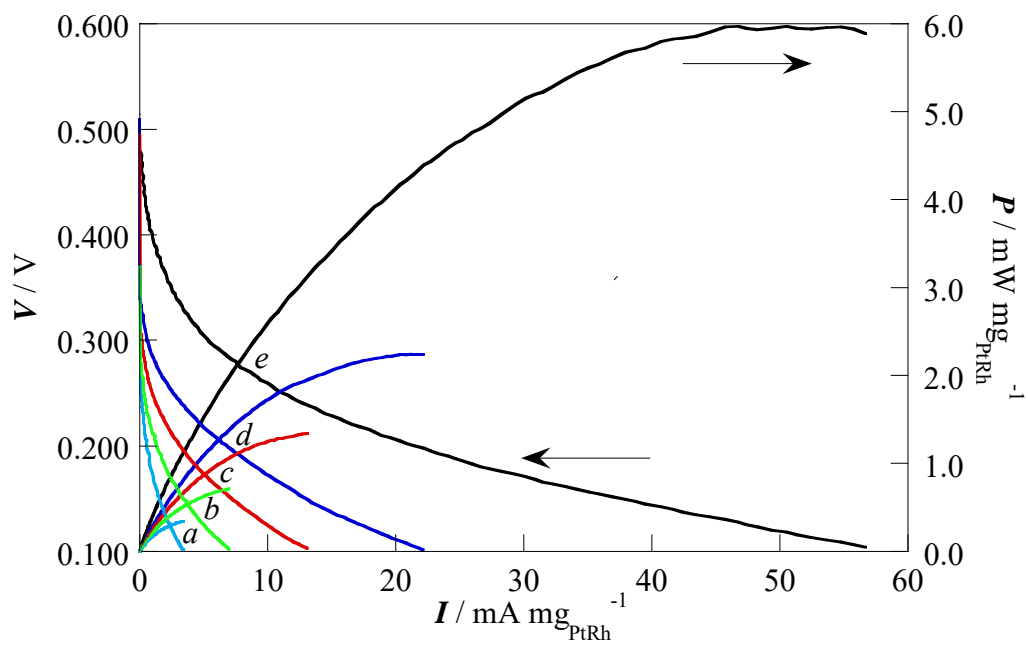


Figure 11